

FLUORESCENCE SPECTROSCOPY

Yin Yeh¹, Samantha Fore,² and Huawen Wu¹

¹*Department of Applied Science, University of California, Davis*

²*Center for Biophotonics Science and Technology, University of California, Davis*

4.1. INTRODUCTION

Fluorescence emission is the result of light having been absorbed and then reemitted at a longer wavelength. In concept, once a material system absorbs the incident light of some energy or wavelength, part of that energy is transferred to the system for various internal conversion needs, and a very short time later the other part is converted to light emission at a slightly lower energy (longer wavelength). The internal transfer part is very rapid and radiationless, but dephasing. So this process is considered a two-photon, three-step, phase-incoherent process.

In this chapter we will discuss (1) the fundamental process of fluorescence, including the factors that can alter fluorescence emission intensity or polarization, (2) the types of fluorescence microscopes used for detecting fluorescent events between molecules and within cells, (3) the types of fluorophores and how they are used, (4) the application of fluorescence features to characterize molecular structures in a biological system, and (5) the exploitation of temporal changes of fluorescence detection for furthering our understanding of structure and dynamics of biomolecular systems. Fluorescence has become a widely used concept in biophysical research. What we will discuss concentrates on specific topics of current interest to the authors. For a complete review, the reader is referred to other volumes, particularly the new edition of Joseph Lakowicz's excellent work [1].

Address all correspondence to Yin Yeh, Department of Applied Science, University of California, Davis, One Shields Avenue, Davis, CA 95616 USA, 530-752-1924, 530-752-2444 (fax), <yyeh@ucdavis.edu>.

4.2. FUNDAMENTAL PROCESS OF FLUORESCENCE

4.2.1. Fluorescence Transition Probabilities

In the classical picture, we describe the process of fluorescence as, first of all, an initial distribution of electrical charges of an atom or molecule being excited by the incident radiation field to reach a state configuration with an electric dipole moment. Upon the radiation field being absorbed by this dipole, the energy of these electrons is used to shuttle the electrons within the electron orbital. The periodical oscillation of an electron over some distance of the orbital will lead to acceleration of these charges. According to the classical description of accelerated charges [2], acceleration and deceleration of these charged electrons will cause light emission. The strength of dipole emission depends on the magnitude of the dipole moment, which is a direct function of the size of the electron orbit.

This classical description, although qualitatively satisfying, does not provide sufficient information about the quantitative nature of the absorption and emission processes. We next treat this problem using semi-classical formalism, whereby the material (atom or molecule) system is treated quantum mechanically, while the radiation field is still considered classical [3]. For simplicity, let us consider a system with only two states described by the wavefunctions, Ψ_1 and Ψ_2 , the ground and excited states, respectively, each being described by the time-independent Hamiltonian, \hat{H} , such that

$$\begin{cases} (\Psi_1 | \hat{H} | \Psi_1) = E_1, \\ (\Psi_2 | \hat{H} | \Psi_2) = E_2. \end{cases} \quad (4.1)$$

If this system is perturbed by a time-dependent interaction Hamiltonian, \hat{H}_I , the new, total Hamiltonian becomes likewise time dependent and can be represented as \hat{H}' , where

$$\hat{H}' = \hat{H} + \hat{H}_I(t). \quad (4.2)$$

In the case of fluorescence, the first step of the interaction Hamiltonian is that between the electromagnetic field of the incident light and the quantum mechanical electric dipole moment, given by the operator $\vec{\mu} = e\vec{r}$. Here, \vec{r} is the coordinate operator for the material system. Hence, the interaction Hamiltonian between the electric dipole in a time-varying electric field of strength \vec{E}_0 , oscillating at the frequency ω , can be written as

$$\hat{H}_I = -\vec{\mu} \cdot \vec{E} = -e\vec{r} \cdot \vec{E}_0 e^{-i\omega t}. \quad (4.3)$$

To fully describe the state of the molecule in this interaction field, it is necessary to determine the rate at which the incident light causes a transition between states. Although we have stated that the fluorescence process is a three-step process, the two radiative transition processes — absorption and emission — can be described using a two-level system that Einstein developed. In this model, the two energy levels, E_1 and E_2 , with their respective occupation numbers, N_1 and N_2 (see Fig. 4.1), may be spanned by the radiation field of frequency ω , with the condition

$$E_2 - E_1 = \hbar\omega > 0. \quad (4.4)$$

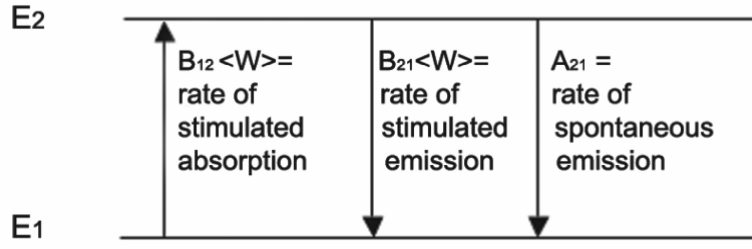


Figure 4.1. Energy level diagram for two-level system described in Einstein's model of atomic absorption and emission. $B_{12}\langle W \rangle$, $B_{21}\langle W \rangle$, and A_{21} are the rates of stimulated absorption, stimulated emission, and spontaneous emission, respectively.

The key point is that when an atom is in the lower state it can be excited to the upper state only if the radiation field satisfies the condition of Eq. (4.4). However, an excited state population will have two possible paths to return to the lower, more energetically stable state: spontaneous emission and stimulated emission. The rates of these processes may be written, respectively, as $B_{12}\langle W \rangle$, $B_{21}\langle W \rangle$, and A_{21} , where $B_{12}\langle W \rangle$ and $B_{21}\langle W \rangle$ are the absorption and stimulated emission rates respectively, while A_{21} is the rate of spontaneous emission. Here, $\langle W \rangle$ is the average energy density of the radiant field imposed. These are referred to as Einstein's A and B coefficients.

In order to compute the values of A and B coefficients for a specific system, it is necessary to look to the quantum-mechanical theory of transition probabilities. In the semi-classical approach, the response of the molecular system to a weak electromagnetic field can be treated with perturbation theory, whereby the eigenstates of the system remain the same, but the effect of the perturbing interaction is a mixing of other states into the initial state, Ψ_1 , to form a final state, Ψ . Here $\Psi = C_1\Psi_1 + C_2\Psi_2$; this state is now the superposition of the original eigenstates each multiplied by time-dependent C_i . The level of mixing into the other states is characterized by the level of exchange between the original state and the final state upon the imposition of H_1 . Thus for the two-level system described above,

$$\langle \Psi | \hat{H}' | \Psi_1 \rangle = C_1(t) \langle \Psi_1 | \hat{H}' | \Psi_1 \rangle e^{-i\frac{E_1}{\hbar}t} + C_2(t) \langle \Psi_2 | \hat{H}' | \Psi_1 \rangle e^{-i\frac{E_2}{\hbar}t}. \quad (4.5)$$

Using the time-dependent Schrödinger equation,

$$\frac{i\hbar d\Psi(t)}{dt} = \hat{H}'\Psi(t), \quad (4.6)$$

the solution to this problem, given the initial constraints of $C_1(0) = 1$, $C_2(0) = 0$, yields the famous *Fermi's Golden rule* [4], which gives the transition rate, Γ , from the initial state, $\Psi_1 = |1\rangle$, to the final state, $\Psi_2 = |2\rangle$, and is shown as follows:

$$\Gamma = \frac{2\pi}{\hbar^2} |\langle 2 | \hat{H}_I | 1 \rangle|^2 \delta(\omega_{21} - \omega), \quad (4.7)$$

where $\omega_{21} = \omega_2 - \omega_1$, with ω_2 , and ω_1 being the angular frequencies representing the energies of the final and initial states, respectively. Therefore, light with frequencies at or near the difference between those of the initial and final states can strongly affect this transition. For the specific case of the dipole interaction discussed above we employ the Einstein B_{12} coefficient, and it is given by

$$\Gamma_{12} = B_{12} \langle W(\omega) \rangle, \quad (4.8)$$

where $B_{12} = \frac{\pi e^2 D_{12}^2}{3 \epsilon_0 \hbar^2}$, D_{12} is the transition dipole moment determined by computing the matrix element $\langle 2|H_1|1 \rangle$ in the analysis above, and $\langle W(\omega) \rangle$ is the averaged radiant energy density of the applied field at frequency ω . It can be further shown that, for this simplified, nondegenerate, two-state system, the rate of stimulated emission from the excited state to the ground state, $\Gamma_1 = B_{21} \langle W(\omega) \rangle$, is equal to Γ_{12} . Thus $B_{12} = B_{21}$, a concept called *microscopic reversibility*. On the other hand, the rate of spontaneous emission, A_{21} , is related to the B_{21} coefficient through the following expression [4]:

$$A_{21} = \frac{\hbar \omega^3}{\pi^2 c^3} B_{21}, \quad (4.9)$$

but is independent of any applied field strength. In this simplified system, and in the absence of a stimulating field, the lifetime of the excited state becomes the radiative lifetime, τ_R , of the spontaneous emission process, which is also called the fluorescence lifetime, τ_F . Thus in this simplified two-state system, $\tau_F = \tau_R = 1/A_{21}$, a very useful experimental parameter in fluorescence-based experiments. For a number of molecules N_2 , initially in the excited state, the rate of deexcitation of molecules by spontaneous emission from that state, is proportional to the product of N_2 and A_{21} :

$$\frac{dN_2}{dt} = -N_2 A_{21}, \quad (4.10)$$

$$N_2(t) = N_2(0) e^{-A_{21}t} \quad (4.11)$$

We now move away from the ideal case of a two-level system into a more realistic molecular system to examine the equivalent absorption and emission processes. First of all, each of the electronic states of the molecule, called the *molecular orbitals*, will contain many possible vibrational states of that molecule [1]. The ground state of an electron in a molecular orbital involved in a fluorescence transition is often referred to as the ground singlet state, S_0 , denoting the fact that its orbital wavefunctions are symmetrical and the spins are paired such that the total spin $S = 0$. Because the electron dipole transition that will lift one electron from S_0 to an upper state must satisfy the electric dipole selection rule, $\Delta l = \pm 1$, but $\Delta s = 0$, the excited state must also exist in the *singlet* manifold. It is often referred to as the excited singlet state, S_1 . Once in the upper state, the electron is jostled around amongst the vibrational states associated with S_1 , and settles in the lowest level, awaiting its decay back to the ground state. The return of this electron when accompanied with its spontaneous emission of electromagnetic field yields the fluorescence emission. This concept is shown in the Jablonski diagram (Fig. 4.2).

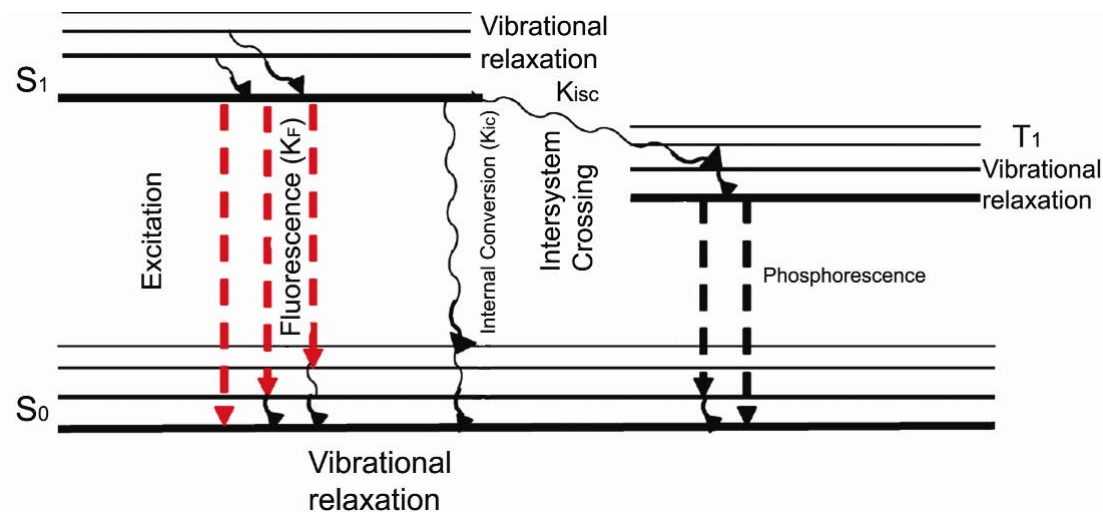


Figure 4.2. Jablonski diagram showing fluorescence decay in the presence of other radiationless, dissipative mechanisms. Please visit <http://www.springer.com/series/7845> to view a high-resolution full-color version of this illustration.

4.2.2. Dissipative Modes of the Excited State

Figure 4.2 shows that, contrary to the two-level model system, there are other nonradiative processes that compete with fluorescence emission — including contributions from vibronic bands within electronic transitions — that have the effect of shortening the excited state lifetime, and shifting the frequency of the emission. The contribution to the lifetime by these nonradiative processes can be characterized by a fluorescence quantum yield. These processes involved are internal conversion (*ic*), where excited state energy is lost via collisions with external molecules or are dissipated through vibrational modes; intersystem crossing (*isc*), where energy is lost by conversion of excited singlet state to the excited triplet state; and other quenching processes (*q*), where collisions or complex formation with species capable of quenching the excited state, such as molecular O_2 , occur. Their respective rates are, k_{ic} , k_{isc} , and $k_q(Q)$. The quantum yield, ϕ_F , is thus given by [5]

$$\phi_F = \frac{k_F}{[k_F + k_{ic} + k_{isc} + k_q(Q)]}. \quad (4.12)$$

Therefore, the observed fluorescence decay time, τ_F , is due to the combination of all these rates.

$$\tau_F = \frac{1}{[k_F + k_{ic} + k_{isc} + k_q(Q)]}, \quad (4.13)$$

and is shorter by a multiplicative factor of the quantum yield, ϕ_F :

$$\tau_F = \phi_F \tau_R. \quad (4.14)$$

Here we have used $\tau_R = 1/k_F$ as the radiative lifetime of the excited state. For most commercially available fluorescent molecules, the fluorescent lifetimes range from 1 to 10 ns, and the quantum yields can vary appreciably, e.g., from 30 to 90%.

4.2.3. Stokes Shift and Emission Spectra

As can be deduced from the above discussion on fluorescence lifetime and from the diagram in Figure 4.2, excitation to and emission from the same singlet electronic states, called resonance fluorescence, rarely happens. As such, the observation of fluorescence emission typically occurs at longer wavelengths (i.e., lower energy) than the excitation wavelength. The common cause of these energy losses is rapid decay from the upper vibrational levels into lower vibrational levels of the excited state, as well as the higher probability for decay into higher vibrational states of the ground state. The vibronic transitions that are superimposed on the electronic states have not been discussed thus far. Electrons involved in molecular fluorescence reside in molecules with their respective chemical bonds, the energies of which can also be quantized as vibrational energy levels. The presence of these vibrational levels is felt by the electrons involved in the electronic transitions. Here, the electronic energy states are superimposed onto the potential energy surfaces corresponding to the nuclear motion (see Fig. 4.3). In the absence of radiation, the lowest vibrational and electronic states are most probable. Since the kinetic energy of the nuclear vibrational motion is zero at points (classical turning points of an oscillator) where the vibrational energy level intersects the potential energy curve, i.e., at points *A* and *B* on the electronic ground state potential energy surface, the electron involved in the transition is most probably found at those positions. Thus excitation most probably occurs from these molecular positions. Likewise, since the transition must conserve kinetic energy as well as lie on one of the quantized vibrational levels, the transition occurs most probably to the position on the excited state potential energy surfaces where the kinetic energy is zero and corresponds to one of the quantized energy levels, point *C* in Figure 4.3a. This is called the Frank-Condon principle, and can be stated as follows [6]: “Since electronic motions are much faster than nuclear motion, electronic transitions occur most favorably when the nuclear structure of the initial and final states are most similar.”

Via thermalization processes and collisions with solvent molecules, a rapid decay into the lowest vibrational state of S_1 occurs. Similar arguments using the Frank-Condon principle can be made with respect to the emission, and thus the electron decays into the vibrational energy level of the electronic ground state with the most similar nuclear configuration, i.e., point *D* in Figure 3a. Quantum mechanically this can be stated in the following manner: the wavefunctions for the initial and final states have the greatest overlap integral. The overall effect with respect to excitation and emission energies is that the latter is smaller, and hence the wavelength of emission is longer. Thus we have the so-called Stokes shift to longer-wavelength fluorescence emission, named after Sir G.G. Stokes, who was the first to observe and describe this phenomenon [7]. An example of the fluorescence excitation and emission spectra for a fluorescent organic dye are shown in Figure 4.3b.

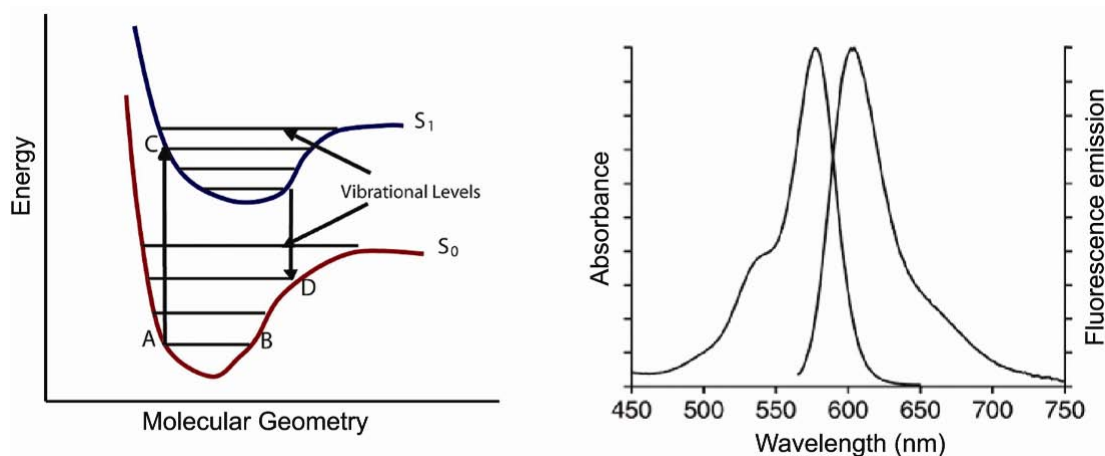


Figure 4.3. (a) Schematic representation of a molecular fluorophore with a wide range of excited- and ground-state vibration levels. (b) These are reflected in typical absorption and emission spectra. Please visit <http://www.springer.com/series/7845> to view a high-resolution full-color version of this illustration.

4.2.4. Multiphoton-Excited Fluorescence

With the availability of coherent excitation light sources, namely lasers, an extremely high intensity of light can be focused onto small sample volumes. The limiting dimension of a laser focal volume is typically a cross-section area of linear dimension X , that of the associated Airy disc [8]:

$$X = \frac{\lambda}{n \sin(\alpha)}, \quad (4.15)$$

and a depth of focus nearly that of the Rayleigh range, z_R , is

$$z_R = \frac{\lambda}{n \sin^2(\alpha)}. \quad (4.16)$$

Here, λ is the wavelength of light in a vacuum, n is the index of refraction of the medium, α is the angle of acceptance, usually defined as $\tan \alpha = d/2f$, where d is the diameter of the lens, and f is its focal length. In microscopy the numerical aperture (NA) is defined as d/f . Thus the focal volume for an objective that has an NA of about 1.0 becomes approximately $(1/4)\pi\lambda^3$. If the light intensity was sufficiently high, the material system might respond via nonlinear coupling to the incident field. High laser intensities delivered in the form of single short pulses into such spatial dimensions can elicit such nonlinear material responses. One of these responses is two-photon excitation (TPE). If the TPE energy is sufficient to excite the ground-state fluorophore into an excited state, then one has achieved the equivalent of single-photon excitation into the same excited state, except now using two lower-energy photons to achieve the same end (Fig. 4.4).

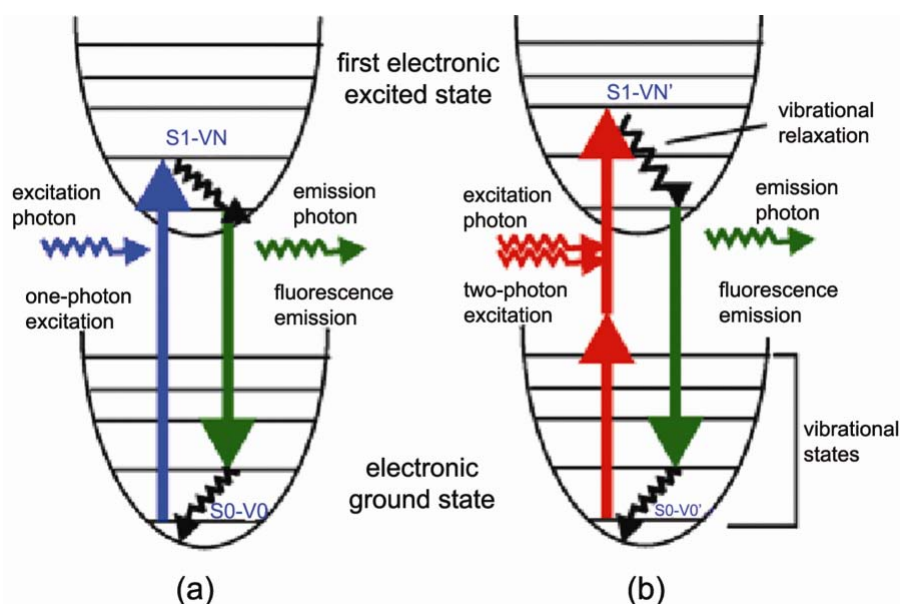


Figure 4.4. Energy-level diagram for single-photon absorption fluorescence (a) vs. two-photon absorption fluorescence (b). Please visit <http://www.springer.com/series/7845> to view a high-resolution full-color version of this illustration.

How does using this process help in monitoring biological fluorescence? Excitation using two lower-energy photons or more (MPE) is a nonlinear optical process. The requirement for successful TPE or MPE is simultaneous impingement of two or more photons onto a spatially localized region. Since each laser excitation beam arrives with its prepared Gaussian beam profile, the product of two Gaussian beams with the same beam profile leads to an excited region that has the same Gaussian profile but with a width roughly half that of the single beam. This provides tighter lateral localization. More importantly, since the nonlinear excitation process requires a higher total energy density to be delivered before the process takes place, whenever the incident beams are not within the focal volume there is not enough energy for effective two-photon excitation. This is illustrated in the Figure 4.5 [9], where axial “sectioning” capability is illustrated. Hence, TPEF or MPEF can be used in a manner similar to the use of confocal microscopy (to be discussed in the following section), achieving optical sectioning, or sampling signals coming from much more spatially localized domains of the sample, one z -layer at a time [10]. This optical sectioning capability allows for achievement of higher spatial resolution.

In the above example depicted in Figure 4.6, the MPEF method employed shows that a single excitation light source can be used to excite a range of dyes [11]. Here, CG-C18 and Indo1-C18 were used to illuminate different domains of a neonatal rat cell. The high spatial resolution achieved shows that the CG dye is mainly confined in the membrane region, whereas the Indo-1 is easily internalized and illuminates regions within the cell. Another advantage of MPEF is that using lower-energy infrared light instead of visible or UV light in direct excitation negates much of the biological sample’s autofluorescence, leading to an image with less unwanted background signal.

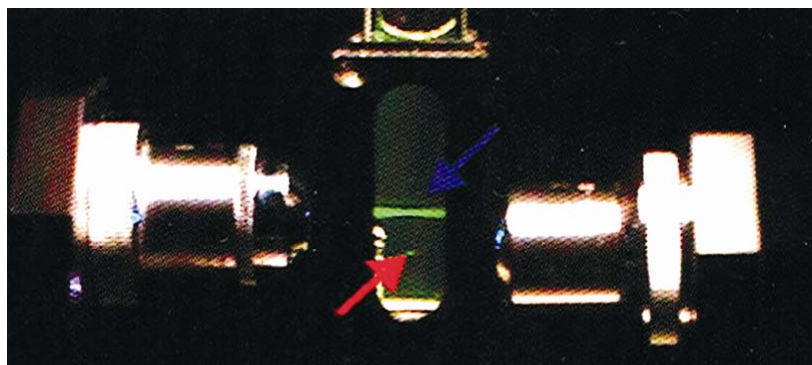


Figure 4.5. Demonstration of the z -sectioning capability of MPEF. Cuvette has fluorophores in solution. Single-photon excited fluorescence is seen throughout the z -length of the laser focus, vs. two-photon excited fluorescence is seen only in very limited z -domain. Reprinted with permission from [9]. Copyright © 1993. Midwest Research Institute. Please visit <http://www.springer.com/series/7845> to view a high-resolution full-color version of this illustration.

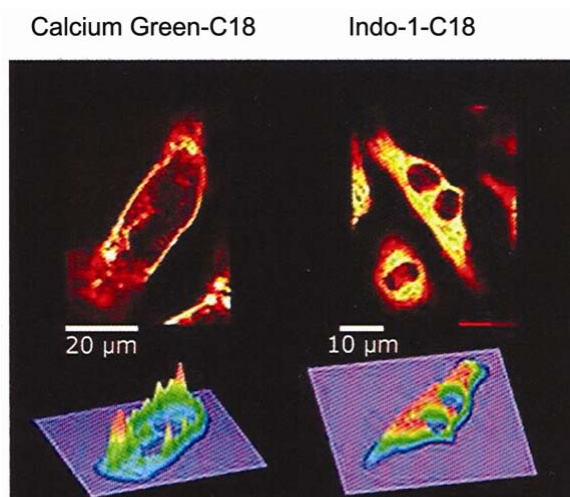


Figure 4.6. Illustration of different dyes accenting different domains of a whole cell can be spatially resolved using MPEF. CG-C18 and Indo1-C18 were employed to illuminate different domains of a neonatal rat cell. (a) CG dye is mainly confined in the membrane region whereas the (b) Indo-1 is easily internalized and illuminates regions within the cell. Reprinted with the kind permission of *Frontiers in Bioscience* [11]. Copyright © 2004, Frontiers in Bioscience Publications. Please visit <http://www.springer.com/series/7845> to view a high-resolution full-color version of this illustration.

4.3. FLUORESCENCE MICROSCOPY

How was the image of the cell shown in Figure 4.6 obtained? Whereas fluorescence signal can be detected in a cuvette (as shown in Fig. 4.5), the sizes of most of the biological entities of interest — cells and molecules — are too small to see clearly in such a system. Hence, we resort to fluorescence microscopy [12]. Figure 4.6 is obtained by using a microscope that exhibits high

spatial resolution, on the order of the wavelength of the exciting light, λ . We discuss three different types of microscopes in the present section: epifluorescence, confocal scanning fluorescence, and total internal reflection fluorescence.

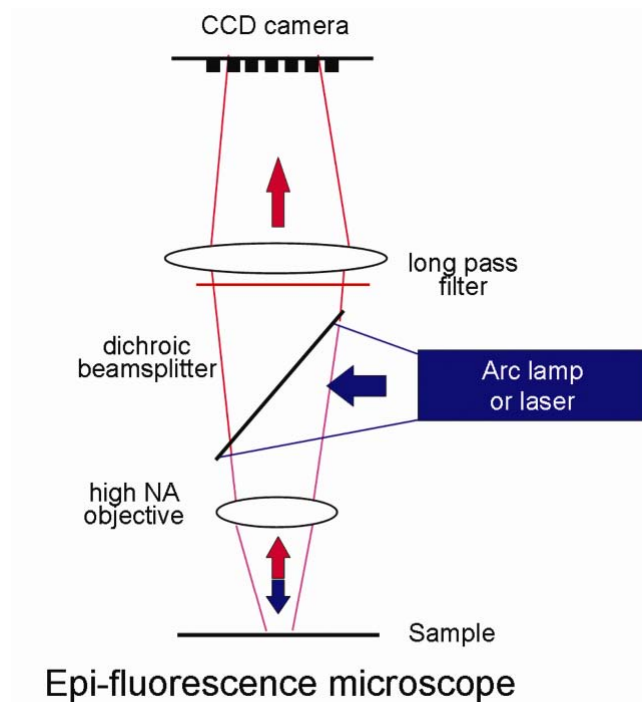


Figure 4.7. Schematic diagram for epifluorescence microscopy. The detector (CCD camera) sees both the in-focus contribution and the out-of-focus contribution as blurred background, reducing the signal-to-noise ratio. Please visit <http://www.springer.com/series/7845> to view a high-resolution full-color version of this illustration.

4.3.1. Epifluorescence Microscopy

An epifluorescence microscope closely resembles a conventional transmission optical microscope. There is a light source used to illuminate a sample of interest. Instead of being a broad-wavelength or white-light condenser lamp, epifluorescence microscopy has as its exciting light source a well-filtered, spectrally “pure” light or a laser. Instead of coming in from the condenser side, the epi-mode of illumination is achieved through the microscope’s own objective lens (Fig. 4.7).

Using a dichroic mirror that passes the excitation light on its way to the sample and passes only the Stokes-shifted fluorescence light on the return path, the objective is used twice: for excitation as well as for collection of the fluorescence signal. Due to the high numerical aperture (NA) of the microscope objectives ($NA > 0.5$), the collection efficiency is very high. The object magnification factor is the product of the magnification factor of the objective — e.g., 10×, 20×, 40×, 63×, 100× — and that of the eyepiece or camera, usually at least 10×. It is therefore possible to gain an overall magnification factor of 1000×! The use of epifluorescence allows imaging

of fluorescently labeled elements of micron-sized objects such as cells at very high resolution (submicron). The chief problem with the epifluorescence mode of microscopy is that, should the region of interest be filled with complex, but also fluorescent (or autofluorescent) species, the lateral spatial separation and depth resolution are both compromised. Often the image captures much of the out-of-focus components, rendering visibility poor. In order to improve on this aspect of fluorescence microscopy, one usually resorts to confocal scanning microscopy.

4.3.2. Confocal Scanning Microscopy

The construction of the confocal microscope differs from epifluorescence microscopy in two essential features. First, the illuminated region of a sample for use in a confocal scanning microscope is a single point or, due to optical wave diffraction, a region corresponding to the Airy disk \times the Rayleigh range. This region, $\sim(1/4)\pi\lambda^3$, samples only a small fraction of the object of interest, i.e., a biological cell, at any instant of time (Fig. 4.8)

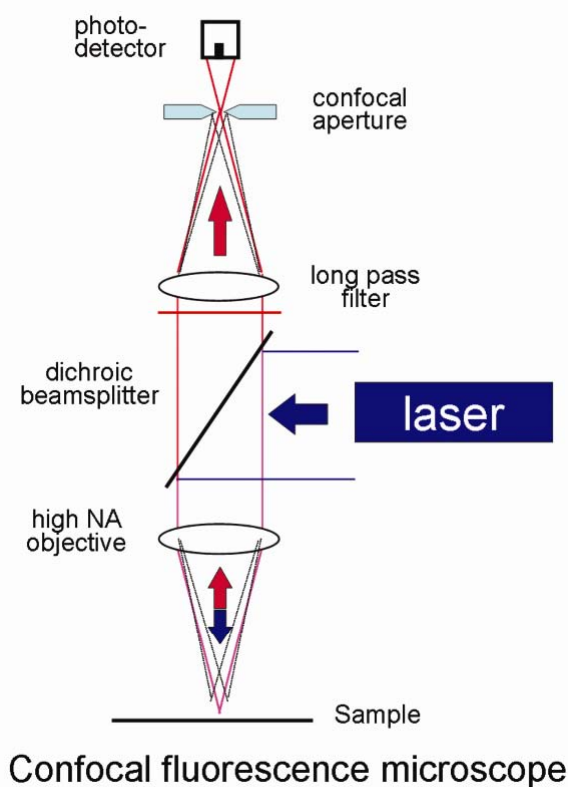


Figure 4.8. Schematic diagram of confocal microscopy geometry. Note the pinhole at the confocal image plane. This scheme reduces not only the out-of-focus noise contribution but allows only the in-focus signal from the pinhole to arrive at the detector. However, sampling is done one spot at a time. Scanning is needed to form an image. Please visit <http://www.springer.com/series/7845> to view a high-resolution full-color version of this illustration.

Light emitted from this region is then focused onto a screen that has, at its confocal position, a matching pinhole. A signal detector lies behind this pinhole to pick up the fluorescent intensity. Because this is detecting only a single point of the object space, in order to create the image of the total object a scanning protocol has to be developed. In the early microscopes, this consisted of raster scanning of the object stage. The intensity at each of the scanned x - y positions is recorded and an image is reconstructed on a screen. Because of the effective double focal volume collection (illumination and pinhole collection), each point sampled has very good spatial resolution, given by $\lambda/(\text{NA})^2$. Similarly, the depth of the sampling is also as good, if not better, leading to true subwavelength resolution for all three coordinates. Because this stage scanning mode is slow and cumbersome, most commercial confocal scanning laser microscopes use a small deflecting mirror that can be moved much more rapidly; hence the rate of confocal scanning microscopy image reconstruction is increased. Furthermore, because the microscope also blocks out out-of-focus light from different z -planes, confocal microscopes have been used to sample depth sections of a thick sample, at a resolution of less than 1 micron.

4.3.2.a. *Optical Sectioning Using TPEF or MPEF*

Let us now return to our discussion of conducting fluorescence microscopy using TPE or MPE excitation. Recall we had stated that the domain of nonlinear optical coupling depends on the intensity of light being delivered to the sample of interest. If the total intensity is below the threshold of TPE or MPE, those fluorophores do not get excited. This concept is identical to that of confocal imaging microscopy. Therefore, TPEF and MPEF are also microscopies that require scanning, but they too exhibit optical sectioning capabilities [13] (see Fig. 4.9).

4.3.2.b. *Spinning Disk Confocal Microscopy*

We have seen the capabilities and advantages of the confocal microscope discussed in the previous section. We have also noted that confocal scanning microscopy is not a “parallel sampling” instrument where every point of the focal plane of interest is sampled in an instant of time. Efforts have been made to overcome the limitations of confocal scanning microscopy. The primary technique is employment of a spinning disk in place of the single focal point. In such a scheme the laser light source is split into multiple optical fibers, each leading to an output independent of the others. At this output plane a disk with many randomly positioned microlenses is placed. The systematic rotation of this microlens array leads to the light source being able to strike each of the many microlenses at one instant of time. So at the focal plane the microlenses will have excited a multitude of sampling points of the object of interest. Hence parallel sampling of confocally illuminated regions is achieved. A system illustrating this scheme is shown in Figure 4.10. Sampling with the high spatial resolution of a confocal microscope but now with high temporal resolution allows probing of dynamic fluorescent events, many of which will be discussed later.

4.3.3. **Total Internal Reflection Microscopy**

When sampling dynamic events of a biological system, conventional confocal scanning microscope is often not rapid enough to catch fast dynamics. If a system, such as a cell, is deposited onto a surface, another approach may be able to rapidly track moving molecules. This

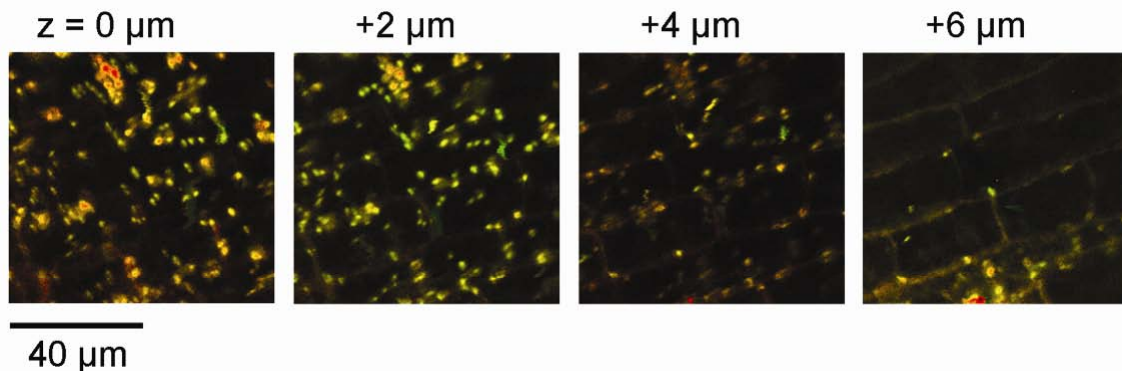


Figure 4.9. Series of two-photon confocal autofluorescence scans through the cotyledon of an *Arabidopsis thaliana* seedling from the organelle-rich interior of the plant cells (0 μm) to the cell wall (6 μm). Please visit <http://www.springer.com/series/7845> to view a high-resolution full-color version of this illustration.

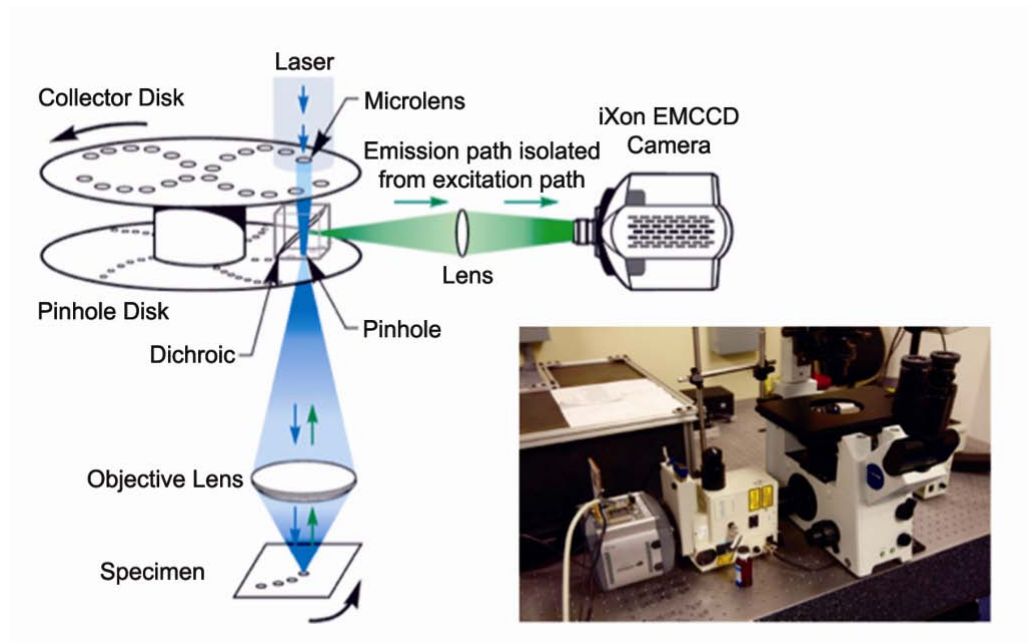


Figure 4.10. Spinning disk confocal microscopy. The multiple set of microlenses and pinholes allows simultaneous illumination of many in-focus confocal spots. Rapid spinning of this random set of pinholes leads to video-rate sampling of confocal images. Please visit <http://www.springer.com/series/7845> to view a high-resolution full-color version of this illustration.

method involves total internal reflection fluorescence microscopy (TIRFM) [14]. When electromagnetic waves contact the boundary of two dielectrics, possessing indices of refractions n_1 and n_2 , the extent of the incident wave that will transmit with refraction and the amount that will reflect into the original medium depends on the angle of incidence as well as the state of polarization. In particular, if light is incident from a denser medium, n_1 , onto a less dense medium, n_2

$< n_1$, there is a critical angle of incidence where there cannot be a transmitted beam in the region of n_2 . Light is thus totally internally reflected. What remains within the medium with n_2 is an evanescent wave that damps out within the lower-index medium over a distance, d , according to the law

$$d = \frac{\lambda}{2\pi\sqrt{\frac{\sin^2 \theta}{n^2} - 1}}, \quad (4.17)$$

where θ is the angle of incidence, which is greater than the critical angle, θ_{cr} , and $n = n_2/n_1$, here always less than 1. For visible wavelengths entering from glass into water, this distance is between 50 and 100 nm. So evanescent layer illumination can be employed to monitor near-surface events without the contribution of particles in the depths of the solution. This is essentially a “tunneling” phenomenon between the initial surface boundary and the presence of the material within the evanescent layer.

If within this damping length a biological molecule is situated, and this molecule carries with it a fluorophore that can absorb the incident wavelength, then wave-tunneling takes place, coupling a part of the evanescent wave to the absorbing molecule. Fluorescence generated from such a TIR tunneling mechanism is called TIRF. Defining a domain where TIR can be satisfied requires the incident angle across the entire outside of the objective to satisfy this TIR condition, so the preparation of a light beam for TIRF differs from confocal microscopy in that the light source must leave the objective (or prism) as a broad, parallel beam. Such an excitation mode naturally creates a much larger domain of illumination. Hence TIRFM can be accomplished with “parallel” sampling in the domain within the evanescent layer. This allows for examining dynamic biological phenomena for molecules or cells lying within this layer near the interface.

Figure 4.11 shows the principle of total internal reflection and the most common approach for achieving TIR conditions. Figure 4.11a shows the condition to achieve total internal reflection, while Figure 4.11b shows that the TIR condition can be achieved by the use of very high numerical aperture objectives ($NA > 1.45$). In this approach, the critical angle can be reached within the objective itself if the incident beam is directed to enter the backplane of the objective from its edge. One advantage of TIRFM is that, due to its tight depth range of illumination, background fluorophores from regions beyond the depth of the evanescent illumination will not be excited, and the only region of the sample illuminated is that nearest to the surface [16].

4.4. TYPES OF BIOLOGICAL FLUOROPHORES

4.4.1. Intrinsic Biomolecular Fluorophore

A feature of dipole emission is that the electron distribution that will create the largest dipole moment, achieved by a large distance of electron traversal, will yield the highest emission field. For delocalized electrons of ring groups in molecular systems, those of the π -bond nature, the emission field will be stronger than that involved with σ -bonds. Consequently, among the

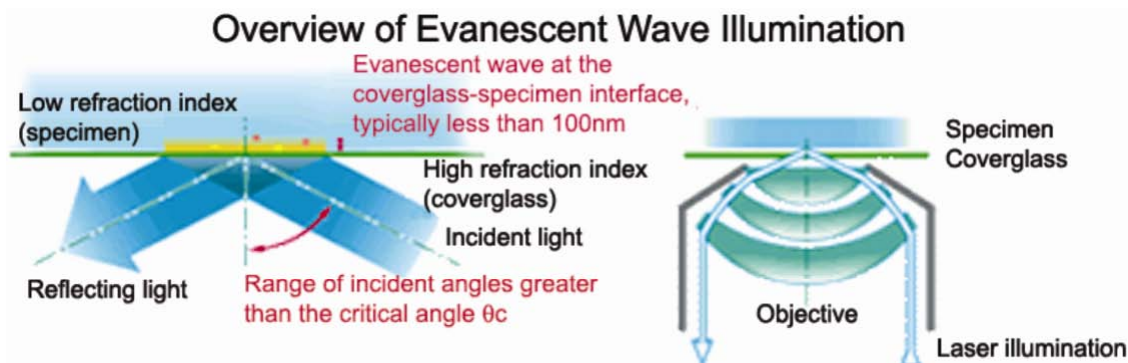


Figure 4.11. The use of total internal reflection (TIR) leads to broad-view sampling a plane within the evanescent layer, thus allowing for microscopy with considerable z -dimension discrimination. Accomplishing TIR fluorescence microscopy using objective excitation and collection is called TIRFM [15]. Please visit <http://www.springer.com/series/7845> to view a high-resolution full-color version of this illustration.

amino-acid residues the ones that are highly absorbing and emitting are the three residues exhibiting ring structures: Tyr, Phe, and Trp. Figure 4.12 shows the molecular schematics of the three residues as well as their respective absorption and emission profiles. Trp is known to be the most efficient intrinsic amino acid emitter residue. However, even at their best, these residues have relatively low quantum efficiencies (~ 0.2).

A second problem concerning the use of intrinsic fluorophores is their pervasive location over the extent of a large protein. If more than one fluorophore can be excited by the incident field, there will be little control to achieve further spatial localization of the emission signal. Consequently, even though the use of these intrinsic fluorophores is least perturbative on the molecular system, their low quantum efficiency and pervasive nature render them not useful except in special circumstances. For example, Trp is a hydrophobic residue often found near the internal hydrophobic domains of a globular protein. The presence of a change in the Trp signal may be indicative of a shifting hydrophobic environment [17].

Another well-known system that is intrinsically fluorescent is the NADH group, which is an enzyme cofactor. It has an absorption peak at 340 nm and an emission peak at 460 nm. Indeed, the change in the autofluorescent signal of NADH provides an indication of the level of oxygen perfusion in tissues [18].

Occasionally, specific defect states of the DNA, such as a bulky adduct lesion created by benzyl[a]pyrene, has its own well-defined absorption and fluorescence signature [19] (Fig. 4.13). Cosman et al. [20] has shown that such a signature is indeed sensitive to the environment wherein the adduct resides, and a full characterization of such DNA adducts provides information about the local environment of the bulky adducts of the benzyl[a]pyrene nature.

4.4.2. Fluorophores Designed for Biological Probes

Extrinsic molecular fluorophores have become a very useful tool for probing for the presence or absence of particular biologically significant species, even though these are introduced as labels

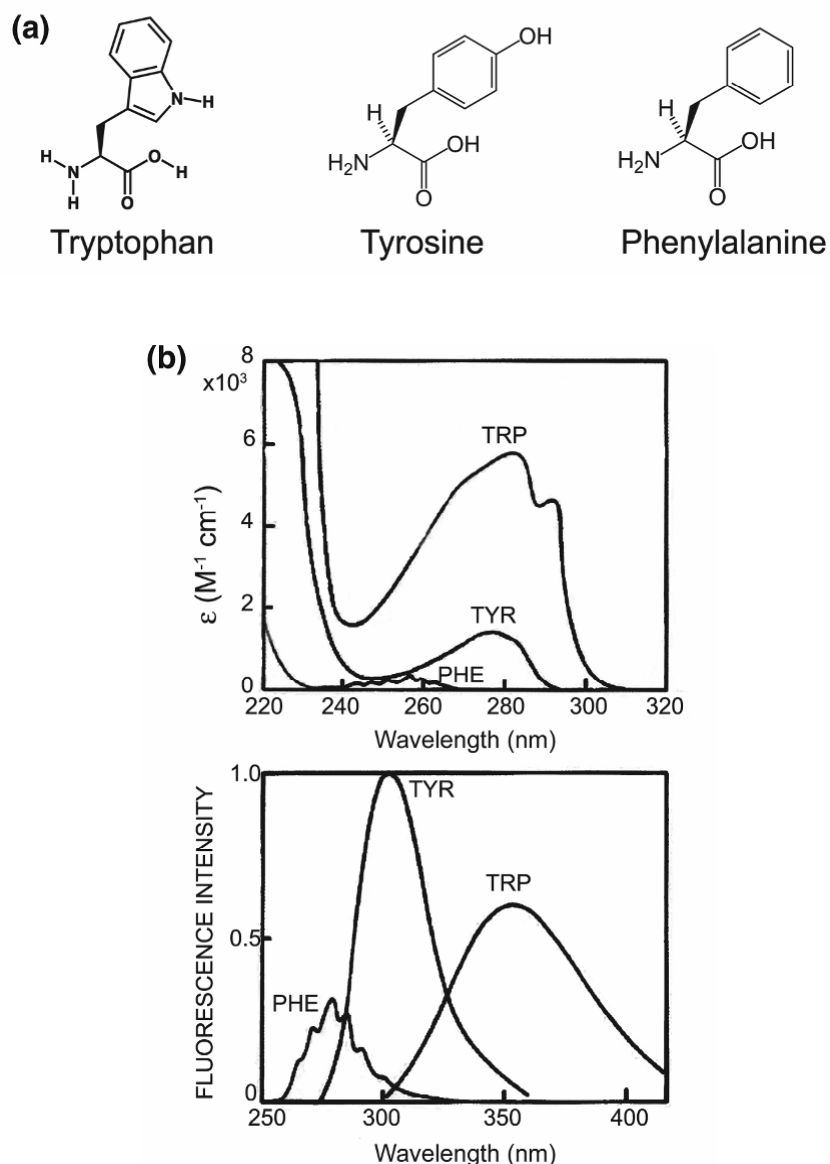


Figure 4.12. (a) Structures of the intrinsic fluorophores amongst amino acids; (b) absorption and emission spectra.

foreign to the cell or molecular systems. Extrinsic fluorophores that exhibit high quantum yields all have large delocalized π -orbitals. The electrons within these orbitals can be easily moved within these delocalized regions to produce large dipoles. Such systems become efficient emitters of fluorescence if their dissipation modes can be controlled. The key to appropriate application of extrinsic fluorophores is to ensure that the functional feature to be probed is not being altered by the presence of the probe. We cite three such systems.

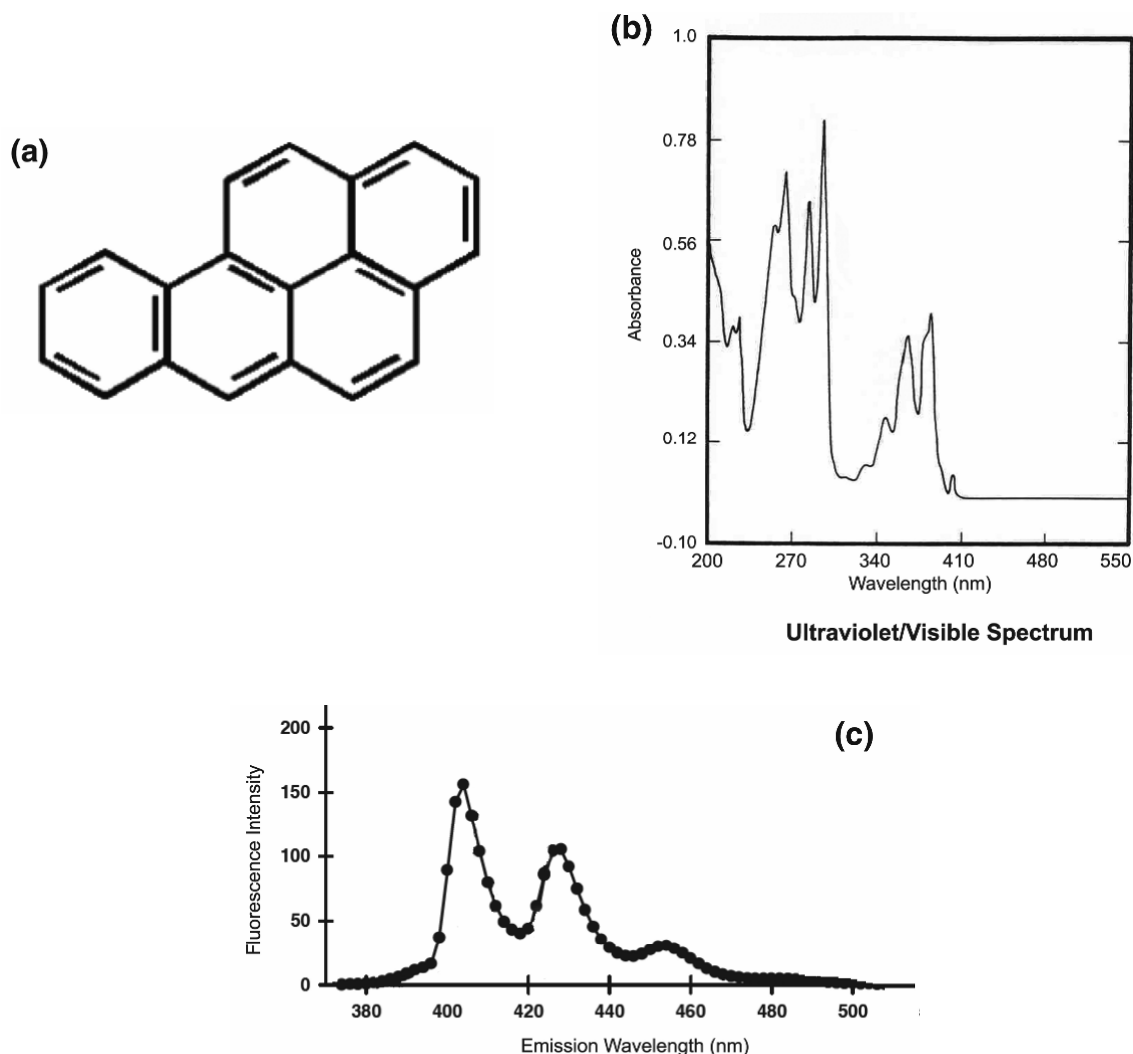


Figure 4.13. (a) Benzo[a]pyrene structure: (b) absorption and (c) emission spectra.

4.4.2.a. Intercalating Fluorophores

Once the probe molecule has been established to have no significant impact on the relevant molecular activity that one is probing, a probe can be made to indicate the presence of a specific state of the biomolecular system. One such fluorophore is the intercalating cyanine dye molecule YOYO-1 [21]. The importance of this probe as an intercalator as opposed to being covalently bound to a part of the DNA molecule is that the ability of the fluorophore to exhibit fluorescence is due to its own structure being “locked” into the base-stacking structure of the dsDNA. The bis-intercalating nature of this molecule is illustrated in Figure 4.14, inserting its large ring domains into the purine–pyrimidine base planes. The stacking energy constraints force the dye groups to be immobile, and thus the locked-in ring groups of this fluorophore de-

rive its high fluorophore emission yield, because there is little room for a dissipation mechanism to develop. However, when the dsDNA is actually opened up and becomes an ssDNA, the dye molecule has no stacking forces, outside some fortuitous same-strand base pairing, to ensure its rigidity. The ring groups in solution will dissipate energy to its environment in a nonradiative manner. The quantum efficiency of this dye drops to 10^{-4} of the fluorophore efficiency when intercalated in dsDNA. This feature is shown in Figure 4.15. Such a simple feature of the dye molecule is then used to identify whether the DNA is indeed in double- or single-stranded conformation.

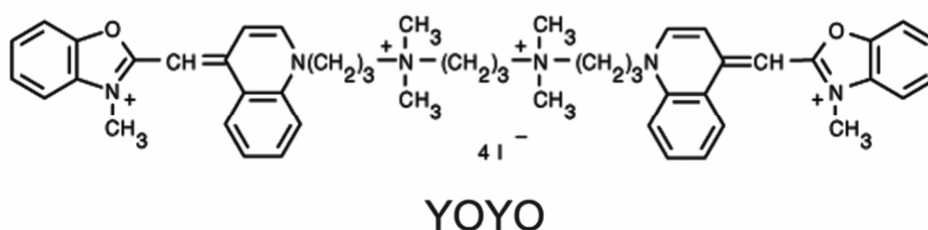


Figure 4.14. The chemical molecular structure of a YOYO molecule showing the double set of ring structures.

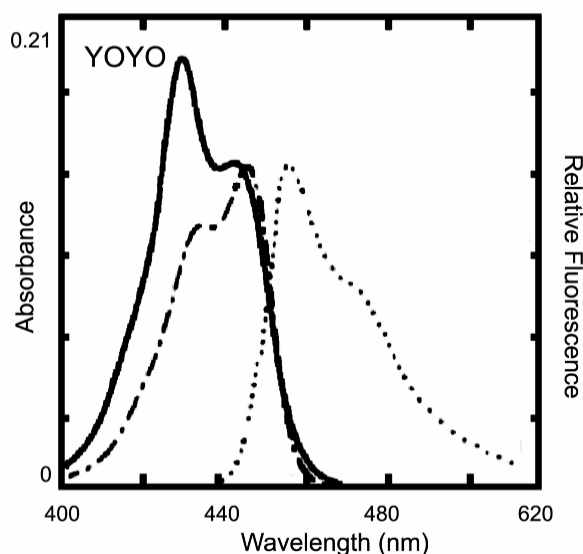


Figure 4.15. Fluorescence spectra of YOYO molecule intercalated into dsDNA: (dot-dashed) abs., (dotted) em. Free dye molecule: (solid) abs., non-detectable em.

4.4.2.b. Membrane Fluorophores

A group of fluorophores that is extremely useful for membrane labeling consists of BODIPY Maleimides, Iodoacetamides, and Methyl Bromides. Because of their lack of ionic charge, these

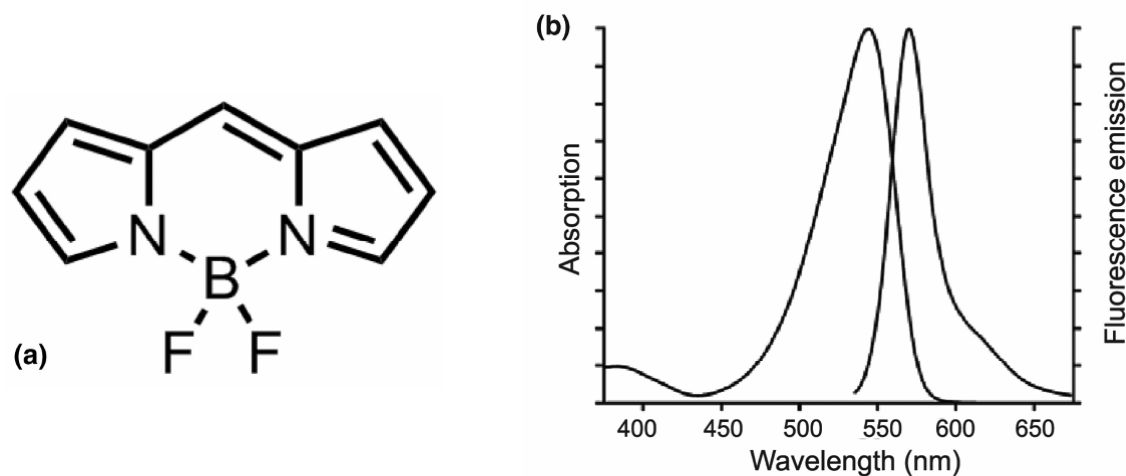


Figure 4.16. BODIPY-FL: (a) structure of BODIPY core; (b) spectrum of BODIPY FL dissolved in methanol

are especially useful when preparing membrane probes and cell-permeant reagents. Several important properties of the BODIPY dyes include (see Fig. 4.16): high extinction coefficients ($>60,000 \text{ cm}^{-1} \text{ M}^{-1}$); high fluorescence quantum yields, often approaching 1.0, even in water; narrow emission bandwidths; good photostability; and a spectrum that is relatively insensitive to solvent polarity and insensitive to medium pH. The BODIPY probes are chemically stable between about pH 3 and 10, although they are less stable in pH extremes than are fluorescein and Alexa Fluor derivatives [1,22].

4.4.2.c. Thiol Labels

Among all the thiol-reactive probes, the Alexa Fluor, BODIPY, fluorescein, Oregon Green, tetramethylrhodamine, and Texas Red derivatives have the strongest absorptivity and highest fluorescence quantum yields. This combination of attributes makes these compounds the preferred reagents for preparing protein and low-molecular-weight ligand conjugates to study the diffusion, structural properties, and interactions of proteins and ligands. The Alexa Fluor dyes exhibit several unique features (see Fig. 4.17): strong absorption, with extinction coefficients greater than $65,000 \text{ cm}^{-1} \text{ M}^{-1}$; excellent photostability, providing more time for observation and image capture than spectrally similar dyes allow; pH-insensitive fluorescence between pH 4 and 10; and superior fluorescence output per protein conjugate, surpassing that of any other spectrally similar fluorophore-labeled protein, including fluorescein, tetramethylrhodamine, Cy3, Cy5, and Texas Red conjugates.

4.4.3. Fluorescent Proteins

In searching for other ways to label proteins to track their location and monitor their dynamics, the discovery of a fluorescent protein that is intrinsic to the jellyfish *Aequoria Victoria* is by far

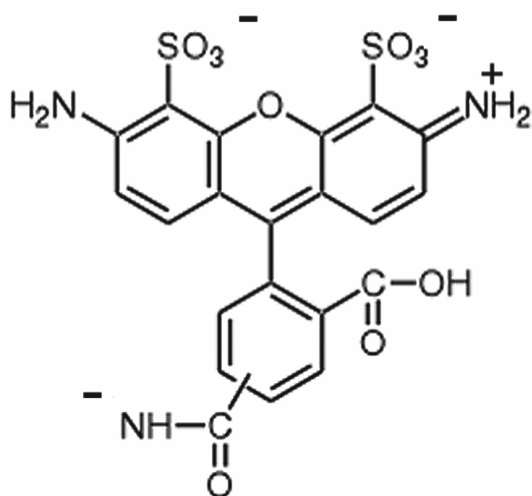


Figure 4.17. Alexa Fluor 488 structure.

the most significant. Having found that a visible fluorescent protein is expressed by an organism through its own genetic makeup led investigators to research the gene of this fluorescent protein. Very shortly afterwards, the gene of the fluorescent protein was found and cloned. This gene can then be transfected into other cellular DNA structures by genetic engineering methods. This led to the ability to create proteins that carry a biological function but is now tagged by this fluorescent protein. Because this protein, in its original construct, emits in the green part of the visible spectrum, it is dubbed green fluorescent protein (GFP) [22]. As can be seen from Figure 4.18, the protein structure is a β -barrel with the fluorophore residing in the middle, hence shielded from the environment. Such a construct is good in that it suffers from very little environmental influence, but due to the bulky barrel housing the protein is rather large in size, and can be a complicating influence should its size place constraints on function or motion of the protein to be reported via this GFP.

The 2008 Nobel Prize in Chemistry was awarded to three scientists — Osamu Shimomura (Marine Biological Laboratory, Woods Hole, MA, USA), Martin Chalfie (Columbia University, USA), and Roger Y. Tsien (UCSD, USA) — for their work in the discovery and development of GFP (http://nobelprize.org/nobel_prizes/chemistry/laureates/2008/). Over the years, the number of variants of GFP has increased. In Figure 4.18b we show the available fluorescent proteins emitting in the entire visible region of the spectrum [23]. Unfortunately, all of these are of the rather bulky variety. So the search for smaller reporters continues.

One such group of reporters that is being intensely studied is the phytochrome. These are much smaller molecular structures found originally in certain plants. Light-sensitive proteins present in photosynthetic organisms contain a protein that is called a “phytochrome.” These proteins allow the organism to adjust to external light conditions. Phytochromes typically contain a nonfluorescent chromophore that can interconvert between two stable forms. When in one of the two stable states, they can combine with phycoerythrobilin, rendering the phytochrome fluorescent in the red wavelength. These proteins also have rather high quantum yields (up to ~ 0.9)

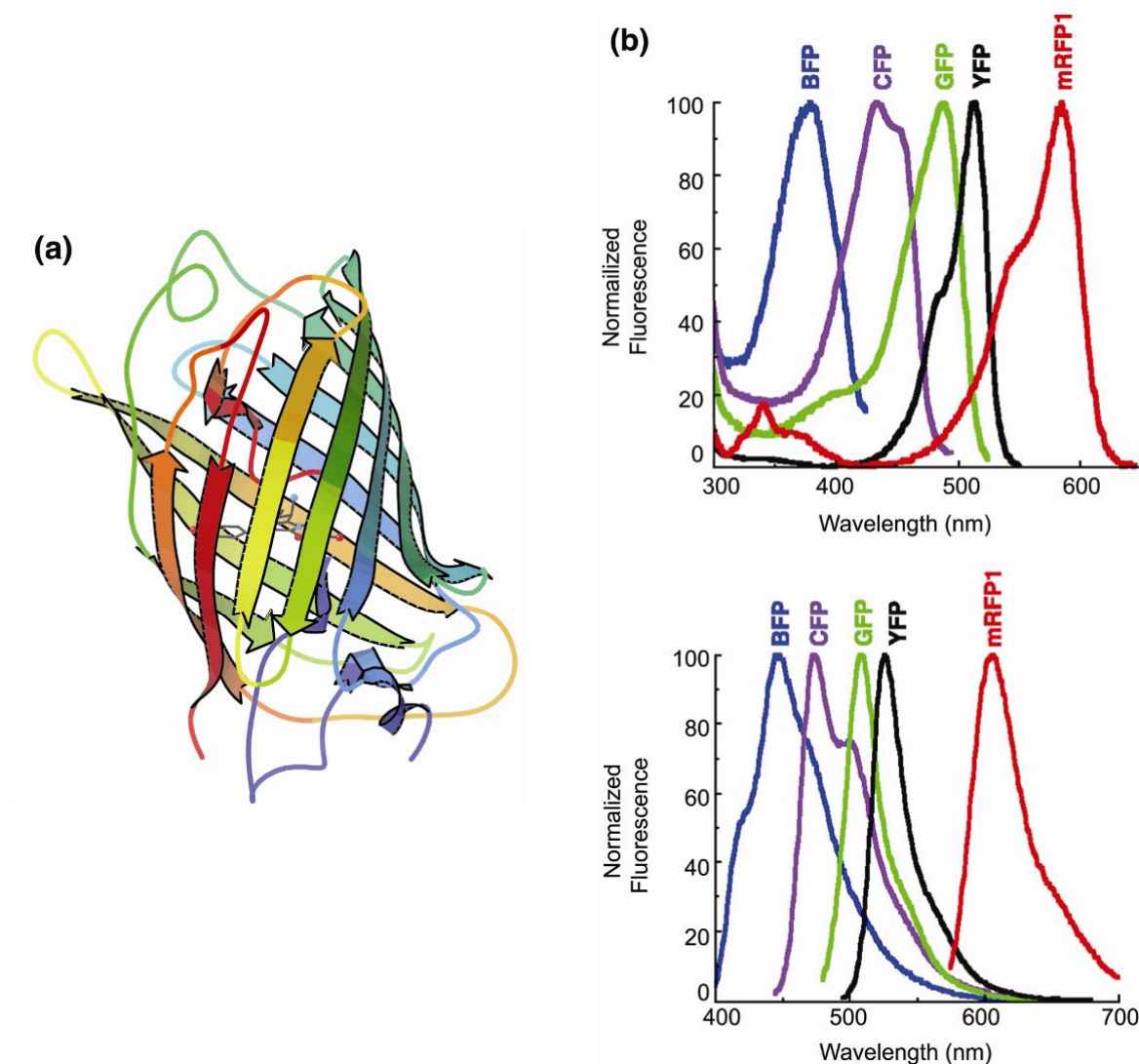


Figure 4.18. (a) Ribbon diagram of GFP in its barrel structure. Rendered from data (ID: IEMA) in the Protein Data Bank (PDB). (b) Absorption (top) and emission (bottom) spectra of variants of the GFP. Please visit <http://www.springer.com/series/7845> to view a high-resolution full-color version of this illustration.

and are up to twenty times brighter and up to tenfold more photostable than fluorescein. Figure 4.19 shows the fluorescent and nonfluorescent variants. The availability of conversion fluorophores means that fluorophores can be made to switch from the “ON” to the “OFF” states. This feature allows possible construction of fluorescent species on demand. Switchable dyes have many other applications, which we will discuss a bit later. Phytochrome apoproteins can be expressed as recombinant proteins [24]. Hence they can be useful as an indicator of gene expression. It is simply a matter of time before these fluorescent phytochromes become another member of the very useful set of expressed proteins with color.

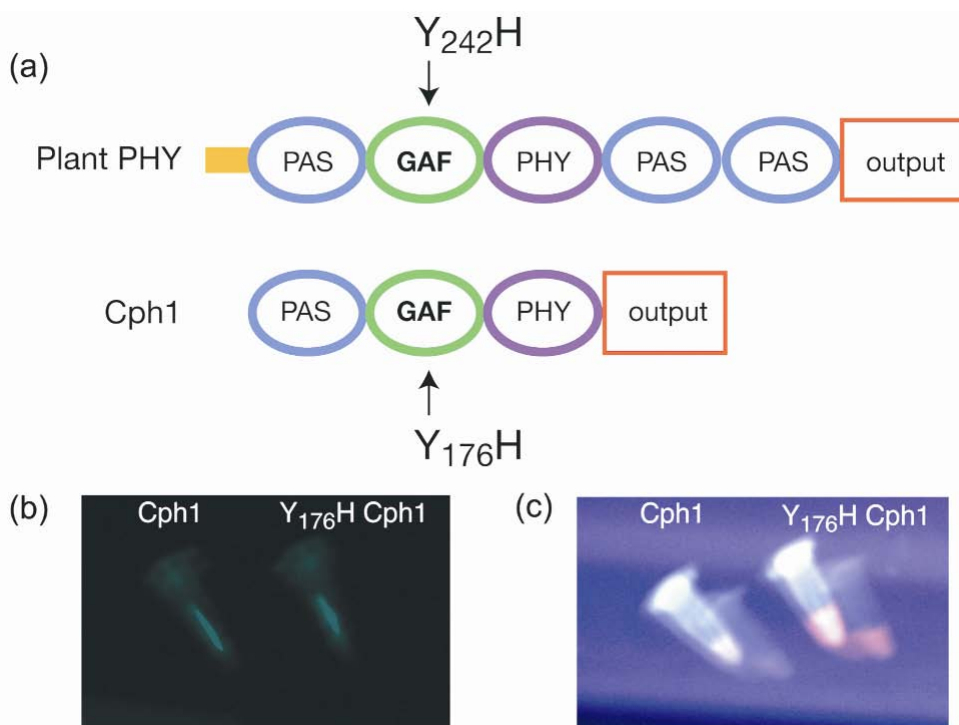


Figure 4.19. (a) Photosensitive domains exist in plant phytochromes (Plant PHY) as well as cyanobacterial phytochrome (Cph1). Specifically in the highly conserved GAF domain, a single amino acid change, from tyrosine (Y) to histidine (H), converts the species from an efficient absorber to an intensely red fluorescence emitter [24]. (b) White light illumination shows little absorption and distinction in emission between the wild type Cph1 and the mutated Y₁₇₆H Cph1. (c) 647-nm light excitation showed that the Y₁₇₆H mutated species are strongly fluorescent in deep red. Courtesy of J. C. Lagarias.

4.4.4. Quantum Dots

A characteristic of the organic dye molecules discussed in the previous sections is their photobleaching properties. As mentioned, a key source of photobleaching is intersystem crossing (*isc*) from the singlet to the triplet manifold within these molecules. In recent years, partly to overcome some of the difficulties of the photobleaching problem, inorganic fluorophores have been explored as a longer-lived substitute. This led to the discovery of the Quantum Dot. As the name implies, this is not a protein reporter but an actual nano-solid that, because of its size, can have its emission spectrum quantized in the same way as energies associated with quantum well structures. By varying the size of the solid material, these energy levels will change, and the cluster or crystalline material will emit light on prescription. These are often rare earth materials where the emission is coming from the delocalized *d*-shell atomic electrons (see Fig. 4.20).

Semiconductor materials such as CdSe, CdS, InP, and InAs with diameters of 3–6 nm have been developed to exhibit intense fluorescence. The wavelength of emission can be adjusted by changing the size and chemical composition of these nanoparticles (NP) or quantum dots (QDots). The optical properties of QDots are similar to those encountered when looking at the

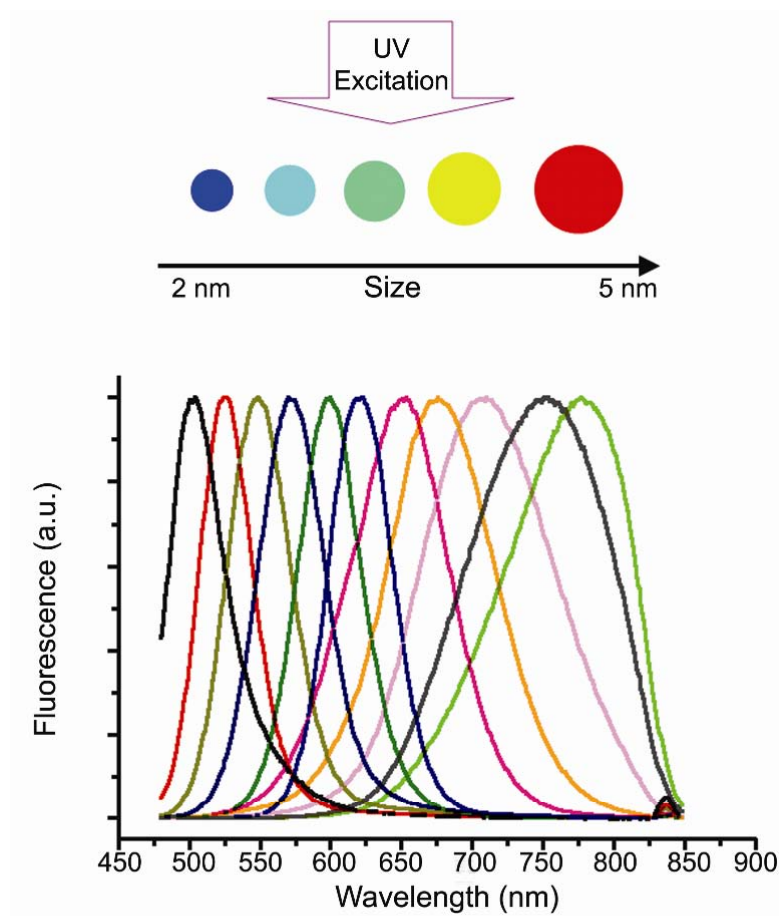


Figure 4.20. Quantum dots. Emission peak depends on the size of the QD. Please visit <http://www.springer.com/series/7845> to view a high-resolution full-color version of this illustration.

problem of a quantum mechanical particle in a box. The size of the box determines the energy level spacing, hence the absorption and emission wavelengths. As a result, great variability in wavelengths of emission can be achieved.

One difficulty in the use of QDots is that most are not water soluble. In order to make the QDots soluble in an aqueous medium, a polymer or silica layer is often used to coat the QDot itself. Once the surface is soluble in nature, the process of making the particle biocompatible and possessing binding specificity is accomplished by the use of sulfhydryl groups. The use of avidin and biotinylated molecules is another approach to specifically labeling a QDot with a biomolecule. The use of a QDot-biocompatible shell structure has been shown to be non-cytotoxic, and can be used as an intracellular probe.

Spectroscopically, QDots have a rather sharp cutoff wavelength at the long wavelength end, and its extinction coefficient is high at shorter wavelengths. Another useful feature is the fact that the fluorescence emission spectrum falls off rather sharply, unlike its organic counterparts. The result of these two features makes QDots a very attractive alternative as an external probe.

Finally, the large extinction coefficient ($\sim 200,000 \text{ M}^{-1} \text{ cm}^{-1}$) makes them very attractive when compared with the extinction coefficient of organic dyes ($10,000$ to $100,000 \text{ M}^{-1} \text{ cm}^{-1}$).

4.5. APPLICATION OF FLUORESCENCE IN BIOPHYSICAL RESEARCH

The general availability of fluorophores that are adaptable for tagging biological molecules and the ability to indicate the tagged location as a visible light source, together with the rapidly advancing technology of light detection and display, have made the use of fluorescence techniques in probing biological events a very widely accepted method for monitoring biological events. In general, these approaches can be divided into two categories: environmental and dynamic probes. We will discuss both.

4.5.1. Use of Fluorescence Environment to Indicate Molecular Activities

As an example, we cite the work of the Kowalczykowski group in identifying molecular events connected with the helicase activity of RecBCD on dsDNA [25,26]. Since the role of the helicase is to open up double-stranded DNA molecules, the important fluorophore to be introduced as a probe of the activity of this helicase must be able to reflect the changing states of the DNA: double- or single-stranded. Since conversion of dsDNA to ssDNA is the indication of a single helicase at work, these studies were able to probe the functional dynamics of a single molecule of the RecBCD enzyme. Thus even steady-state fluorescence signals can be used to characterize biomolecular events, if the activity probed is slower than the fluorophore emission lifetimes.

In this study, single dsDNA molecules of λ -DNA were labeled with the intercalating dye YOYO-1. The amount of label used is decided in order to balance detectability of the molecule and non-hindrance of helicase activity. In order to track the activity of the helicase molecule, the length of the dsDNA must be discernable at all times. An experimental approach used is to attach one end of the λ -DNA by biotinylation to a latex sphere (see Fig. 4.21). Upon optical trapping of this nearly $1\text{-}\mu\text{m}$ -diameter bead, the system is put under a flow condition so that the viscous drag on the dsDNA will extend the molecule, showing a visible track of bright fluorophores fully intercalated into this $15.5\text{-}\mu\text{m}$ λ -DNA. When the RecBCD is introduced to the blunt, free end of such a system, this motor protein is bound to the dsDNA, but nonfunctioning as a helicase. Hence the protein's own visibility is not present. However, the functionality of the RecBCD can be derived by monitoring the change in length of the fluorescently labeled dsDNA. This is achieved by introducing Mg:ATP into the flowcell and by tracking the change in length of the dsDNA on a CCD camera. Since ssDNA, that which has been opened by the RecBCD helicase, has a much smaller propensity for the YOYO-1 dye molecule because of its minimum ability to reassociate as stacking pairs, the fluorescent signal of the YOYO-1 molecule drops into solution. As we have shown in the previous section, the solution environment renders YOYO-1 dye essentially invisible. Thus the changing length of the dsDNA is an indicator of the dynamic processivity of the motor protein complex RecBCD.

4.5.2. Fluorescence Lifetime Spectroscopy

Equations (4.12)–(4.14) suggest that the quantum efficiency of a given fluorophore is related to many of its dissipation processes. We mentioned that this is simply energy conservation: if the excited system does not return its energy via the radiative (fluorescence) route, it is giving up its

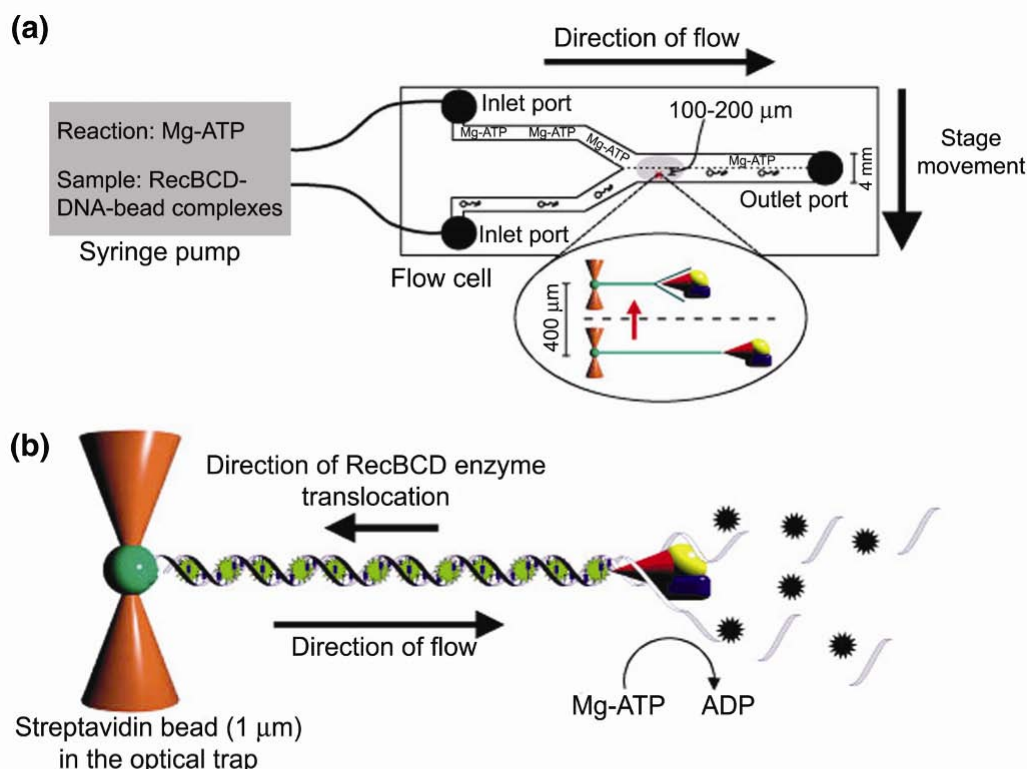


Figure 4.21. (a) Experimental design with syringe pump and flow cell. The sample syringe contains helicase–DNA–bead complexes, and the reaction syringe contains ATP. The red arrow indicates movement of the trapped DNA–bead complex across the boundary between solutions. (b) Fluorescent DNA helicase assay. As RecBCD enzyme translocates, it both unwinds and degrades the DNA, simultaneously displacing dye molecules. Reprinted with permission from [25]. Copyright © 2001, Nature Publishing Group. Please visit <http://www.springer.com/series/7845> to view a high-resolution full-color version of this illustration.

energy to other paths. Significantly, experiments designed to obtain information about these pathways of returning the excited-state energy to its ground state is providing valuable insight into the processes of molecular dynamics. We shall explore a number of these in this section.

In the previous section, we discussed one type of internal conversion. The excited-state energy of YOYO molecules is vibrationally dissipated to their aqueous environment. Hence we used that as an indicator of the state of the molecule being probed, which in that case is dsDNA. Other modes of internal conversion can include electron transfer, of which the guanine residue is an excellent example. Fluorophores closely associated with a G base tend to lose their fluorescence efficiency via this excitonic exchange process—called Photoinduction Electron Transfer or PET [27,28]. The Sauer group has shown that the spatial range for efficient PET is only around 2 nm. So the temporal change in fluorescence signal can be used to characterize very short ranges of interaction.

Another type of conversion process is when the excited singlet state undergoes an intersystem crossing, leaving the electron in a triplet manifold excited. Since triplet and singlet manifolds differ by their electronic spin, $\Delta S = 1$, and the electric dipole (E_1) radiation process associ-

ated with fluorescence does not require spin change, those electrons transferred via this *isc* process do not return to their ground state ($S = 0$) radiatively with any rapidity. In fact, the radiative process from the triplet manifold to the ground state needs to be accompanied by significant spin–orbit interaction. The rate of return is directly related to the strength of the spin–orbit interaction. Because this interaction is weak, the associated radiative decay process is also a slow process, sometimes called “phosphorescence,” usually occurring in the millisecond range or longer. The third transfer process is via excited-state resonance energy transfer to another fluorophore, either intra- or intermolecular. We discuss that in the following section under the rubric of fluorescence resonance energy transfer.

Within the remaining part of this section, we introduce the notion that measuring the lifetime of fluorescence sometimes is another effective way of obtaining similar information about the various paths that excited-state electrons can take. This is called fluorescence lifetime spectroscopy. In a solution environment that is homogeneous to all of the fluorophores, monitoring such a process usually requires a pulse–probe approach. A single pulse of excitation is given; subsequently, the decay process lifetime is monitored by following fluorophore decay. As seen in Eq. (4.13), all of these processes we have discussed will affect the decay time. The dominant ones will be those measured by this process. Detection of the lifetime of fluorophores, which are typically in the nsec regime, requires modern systems with fast electronics, one of which being Fluorescence Lifetime Imaging Microscopy (FLIM). In such a system, emission from individual fluorophores is recorded along with a time tag. The decay of the tagged fluorophores is then monitored as a lifetime signature for that signal. All of the time, tagged and spatially tractable fluorophores are then stored in memory and displayed on a screen as a function of their lifetimes. This lifetime imaging of fluorophores, particular for intracellular domains, provides a means to assess the different environments that specific fluorophores encounter within a cell. If the fluorophores are tagged onto or are native to specific intracellular molecules of interest, this method can provide new information about localized environmental conditions.

4.5.3. Fluorescence Anisotropy

Even if one has chosen to be careful in the mode of excitation, and is in full control of the fluorophore’s environment so that we know the limiting lifetime is from the radiative process of interest, we can still extract more information by *polarization monitoring*. Imagine the system being excited by a pulse of light that has a distinct state of polarization. We expect that in the initial rapid *ic* process the state of excited polarization is somewhat, but not randomly, altered. Now, within the given fluorescence lifetime, suppose the fluorophore undergoes rotational motion. The emission dipole will subscribe to that motion. If the detector monitors a distinct state of polarized fluorescence emission, then this rotational process of the molecule will lead to observable change in the polarized emission intensity. This is called fluorescence depolarization via molecular rotation. In sampling the fluorescence anisotropy, the experimental design sends polarized light into the sample. At the collection angle, usually 90° so as to be away from the strong forward scattering contribution, a polarizer is placed before the detector. A Wollaston Prism produces two polarizations at geometrically symmetrical angles relative to the axis of the prism. Collecting the light from both polarization directions allows for measurement of the quantity called the Anisotropy Ratio:

$$r = \frac{I_{\parallel} - I_{\perp}}{I_{\parallel} + 2I_{\perp}}. \quad (4.18)$$

We can see from this expression that the difference in the intensity of the polarized light in the two directions of polarization is tied to the total fluorescent intensity; hence, the quantity r is independent of the instantaneous intensity fluctuations due to source instability or fluorophore concentration effects. In order to obtain information about the changing nature of fluorescence anisotropy in time, $r(t)$ is measured. In principle, the analysis considers movement of a fluorophore, or the molecule to which the fluorophore is rigidly attached, to execute rotational motion in its environment. If the fluorophore is simply executing rotational Brownian motion, then

$$r(t) = r_0 e^{-\frac{t}{\theta}}, \quad (4.19)$$

where r_0 is the initial time anisotropy ratio, and θ is the rotational diffusion coefficient of the rotor representing the molecule or fluorophore. A complete analytical solution for this process was developed by Weber [29,30]. The fluorophore that tags the molecule of interest often has its typical nsec fluorescence lifetime, but the molecule being probed is rotating or tumbling at a much slower rate due to its much larger size. In order to use this method of monitoring fluorescence anisotropy for these slower events, such as that encountered in myosin subfragment-1 ($S-1$) dynamics during muscle contraction processes, investigators have used phosphorescence anisotropy as a probe. Because the lifetime associated with the process of phosphorescence is sometimes even milliseconds, the rate-limiting step is the myosin $S-1$ dynamics, no longer the lifetime of the fluorophore itself. Triplet state transient dichroic absorbance (TDA) from T_1 to T^* states via a second light source that induces absorption within the triplet manifold is another way to achieve the same rotational information [31].

4.5.4. Photobleaching and Methods to Overcome

Photobleaching is the result of an unavoidable pathway for the excited states of molecules to dissipate its energy. The rate of this process is usually given by k_{isc} . In the previous section we showed two ways the unavoidable process has been used to advantage in probing biological processes. From an energetic standpoint, if the triplet state becomes occupied the most efficient way is to introduce some new way by which the fluorophores locked into the triplet state can quickly return to the ground, singlet state. The original developers of the dye laser had to contend with this situation in order to ensure an efficiently operating dye laser. The use of molecular singlet O_2 or other agents such as mercaptoethylamine (MEA) has been considered an effective remedy against photobleaching. The main idea is to introduce a species that can interact with the triplet-state molecular system, thus driving it back to its ground state, without adversely affecting the singlet-state population.

In defeating the negative features of photobleaching, Koppel and Axelrod have developed a method of “going with the crowd,” where one allows the photobleaching process to take place, and then following the return in space or polarization state, the recovery of fluorescence. This is called “fluorescence recovery after photobleaching” (FRAP) [32]. We will discuss that method as a way of obtaining dynamic information via fluorescence in the next section.

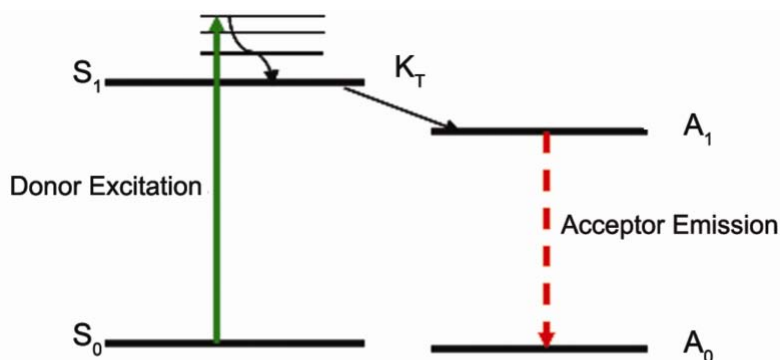
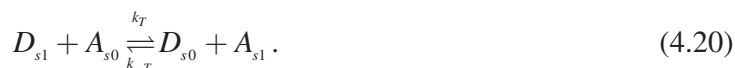


Figure 4.22. Donor and acceptor deexcitation and excitation, respectively. Opposite reaction, i.e., k_{-T} does not occur because both donor and acceptor rapidly relax via vibrational interactions. Please visit <http://www.springer.com/series/7845> to view a high-resolution full-color version of this illustration.

4.5.5. Fluorescence Resonance Energy Transfer

Qualitatively, fluorescence resonance energy transfer (FRET) is the nonradiative energy transfer from a donor molecule excited state to an acceptor molecule, thus raising it to its respective excited state. Thus excitation of the donor molecule is quenched and emission from the acceptor molecule is observed. The interaction can be described by the following reaction (see depiction in Fig. 4.22):



Two physical conditions must exist for this process, which can be considered a weak coupling of the donor and acceptor electronic states, to occur. First, the energy of the donor excited state must be coincident with the transition energy of the acceptor ground and excited states. Second, the donor and acceptor transition dipole moments must have some amount of overlap, i.e., the more aligned the dipole moments are, the stronger the interaction. The former manifests itself in the degree of overlap between the donor emission spectrum and the acceptor absorption spectrum. Thus FRET is physically a case of dipole–dipole coupling, and depends on the spatial orientation of the two molecules with respect to each other. The rather short-range distance dependency of the transfer efficiency comes about directly from the concept of dipole–dipole interaction, which yields a dependence of $1/R^6$. This provides a powerful means for characterizing molecular distances in biological systems. We briefly describe below how the energy transfer efficiency explicitly depends on the spatial distance and the orientation of the two molecules using a theory developed by Theodore Förster [33]. Explicitly for FRET we are interested in the rate at which the donor–acceptor pair changes from the coupled wavefunctions $|\psi_{D_{s1}}\psi_{A_{s0}}\rangle$ to $|\psi_{D_{s0}}\psi_{A_{s1}}\rangle$ via the dipole–dipole interaction described above. We thus have

$$k_t \propto \left| \langle \psi_{D_{s0}}\psi_{A_{s1}} | \hat{H}_I | \psi_{D_{s1}}\psi_{A_{s0}} \rangle \right|^2, \quad (4.21)$$

where the interaction Hamiltonian describes the dipole–dipole interaction potential, V , which can be expressed in terms of a multipole expansion as

$$\hat{H}_I = V = \frac{\vec{\mu}_D \cdot \vec{\mu}_A}{R^3} - \frac{3(\vec{\mu}_D \cdot \vec{R})(\vec{R} \cdot \vec{\mu}_A)}{R^5}, \quad (4.22)$$

where $\vec{\mu}_D$ and $\vec{\mu}_A$ are the donor and acceptor dipole moments, respectively, and R is the distance between the donor and acceptor molecules. Carrying out dot product operations in the above expression, and lumping all of the orientational terms into the parameter κ , V can be rewritten as

$$V = \frac{\kappa |\vec{\mu}_D| |\vec{\mu}_A|}{R^3}. \quad (4.23)$$

Substituting this expression for V into the formula for k_T ,

$$k_t \propto \left| \frac{\kappa}{R^3} \langle \psi_{D_{s0}} \psi_{A_{s1}} | |\vec{\mu}_D| |\vec{\mu}_A| | \psi_{D_{s1}} \psi_{A_{s0}} \rangle \right|^2. \quad (4.24)$$

Since $\vec{\mu}_D$ and $\vec{\mu}_A$ depend only on the electronic coordinates of the donor and acceptor molecule, respectively, we can factor the expression accordingly to

$$k_T \propto \left(\frac{\kappa^2}{R^6} \right) \left| \langle \Psi_{D_{s0}} | \mu_D | \Psi_{D_{s1}} \rangle \right|^2 \left| \langle \Psi_{A_{s1}} | \mu_D | \Psi_{A_{s0}} \rangle \right|^2. \quad (4.25)$$

The expectation values in the expression above correspond to the value of the transition dipole moments, D_{12} , as described above in the general section on fluorescence. In the case of absorption, the square of this has been shown to be inversely proportional to the frequency [34] — that is, for acceptor absorption,

$$D_{12}^2 = \left| \langle \Psi_{A_{s1}} | \mu_D | \Psi_{A_{s0}} \rangle \right|^2 \propto \varepsilon_A \nu^{-1}, \quad (4.26)$$

where ε_A is defined as the molar extinction coefficient and is related to the B_{12} coefficient derived above. For the case of the donor transition, we make use of the relationship between B_{12} and A_{21} given in Eq. (4.10) above, and find that

$$D_{12}^2 \propto A_{21} \nu^{-3} = \tau_R^{-1} \nu^{-3}. \quad (4.27)$$

Using the relationship between the excited-state lifetime and the radiative lifetime as given above in the section on quantum yield, we obtain

$$\left| \langle \Psi_{D_{s0}} | \mu_D | \Psi_{D_{s1}} \rangle \right|^2 \propto \frac{\phi_D}{\nu^3 \tau_D}. \quad (4.28)$$

Combining both of these results for the transition dipole moments, the rate of energy transfer can now be expressed as

$$k_T(\nu) \propto \left(\frac{\kappa^2}{R^6} \right) \left(\frac{\phi_D}{\tau_D} \right) \varepsilon_A \nu^{-4}. \quad (4.29)$$

Since in reality both acceptor absorption and donor fluorescence occur over a band of frequencies due to the vibrational levels, it is necessary to integrate over the entire applicable frequency range. First, let $f_d(\nu)$ be the normalized donor fluorescence spectrum. Then the total rate of energy transfer is computed by integrating:

$$k_T \propto \left(\frac{\kappa^2}{R^6} \right) \left(\frac{\phi_D}{\tau_D} \right) \int \varepsilon_A(\nu) f_d(\nu) \nu^{-4} d\nu = \left(\frac{\kappa^2}{R^6} \right) \left(\frac{\phi_D}{\tau_D} \right) J, \quad (4.30)$$

where J is referred to as the overlap integral.

In summary, the following properties of FRET have been elucidated via the above discussion. The rate of energy transfer decreases rapidly with increasing donor–acceptor distance, i.e., at a rate proportional to R^{-6} . Another aspect of this expression is the angular factor, κ . Because both emission and absorption are electric dipoles, their relative orientation plays a role in the degree of effective coupling between donor and acceptor. When this factor is averaged over all angles, we have $\chi^2 = 2/3$, a number often used in these experiments. The rate depends on the amount of spectral overlap between donor emission and acceptor absorption, i.e., proportional to J , the overlap integral. Finally, the rate also depends on the individual probabilities of absorption and emission of the acceptor and donor, respectively, and these respective rates are characterized by an acceptor molecule's extinction coefficient, ε_A , and a donor molecule's quantum yield, ϕ_F , and excited-state lifetime, τ_D . It is useful to define a characteristic transfer distance, R_0 , the so-called Förster distance, such that the rate of energy transfer can be written as

$$k_T = \left(\frac{1}{\tau_D} \right) \left(\frac{R_0}{R} \right)^6. \quad (4.31)$$

The above discussion on the rate of energy transfer yielded the relation of k_T to the physical parameters of the system, that is, the spectral and spatial parameters of the donor and acceptor molecules. The actual expression for k_T can be calculated by factoring in the various physical constants in the equations for Fermi's Golden Rule and the Einstein coefficients B_{21} and A_{21} , and is given by

$$k_T = 8.79 \times 10^{-5} \left(\frac{\kappa^2 n^{-4}}{R^6} \right) \left(\frac{\phi_D}{\tau_D} \right) J, \quad (4.32)$$

where J has been converted to a wavelength scale using $\lambda = c/\nu n$, with wavelength units of nanometers, that is,

$$J(\lambda) = \int \varepsilon_A(\lambda) f_d(\lambda) \lambda^4 d\lambda, \quad (4.33)$$

where $J(\lambda)$ is in units of $\text{nm}^4 / \text{M} \cdot \text{cm}$

We can then factor out terms to define R_0 as,

$$R_0 = \left(8.79 \times 10^{-5} \kappa^2 n^{-4} \phi_D J(\lambda) \right)^{\frac{1}{6}} \quad (\text{in Angstroms}). \quad (4.34)$$

A useful experimental parameter that can be observed from FRET measurements is the energy transfer efficiency, E . The efficiency of energy transfer is defined as

$$E = \frac{k_T}{k_T + \tau_D^{-1}}. \quad (4.35)$$

Using the expression for k_T in Eq. (4.27), E can also be written as

$$E = \frac{R_0^6}{R_0^6 + R^6}. \quad (4.36)$$

We therefore have two situations that exist when $R = R_0$, $k_T = 1/\tau_D$, and $E = 0.5$. R_0 for typical donor–acceptor FRET pairs ranges from about 1.0 to 10.0 nm. This distance range is comparable to the typical size of many biomolecules — e.g., proteins and DNA — as well as the distance of interaction between different molecules. This technique thus lends itself very nicely to biological experiments. There are several concerns in achieving full utilization of FRET for measuring molecular distances. One key element is the spectral overlap between donor and acceptor molecules (spectral crosstalk). A second relates to orientational averaging for the dipole orientations, the donor as well as the acceptor. As a result, it is often difficult to obtain quantitative information from FRET measurements in bulk biological samples. Several control experiments and significant analysis must often be conducted to even obtain a qualitative picture of the FRET process for a particular system [35,36]. Most of the advances in this area have been in the area of better handling of the spectral crosstalk problem. We discuss in some detail one of the most useful approaches below.

4.5.6. Pulsed Interleaved Excitation FRET

Single-molecule FRET, or single-pair FRET (spFRET) as it is often called, was first developed for biological applications by Ha et al. [37]. It has been used to investigate protein folding, binding interactions, conformational changes, etc., at the single-molecule level. Due to the inherent absence of ensemble effects, the problems mentioned above are minimized when analyzing the FRET interaction between a single donor and a single acceptor molecule. Here, the key consideration is indeed spectral crosstalk. In the first spFRET experiments, single-laser excitation of the donor molecule was used, and the subsequent fluorescence emission intensities of the donor and acceptor molecules were used to calculate the energy transfer efficiency, E :

$$E = \frac{I_a}{I_a + I_d}. \quad (4.37)$$

where I_a and I_d are the intensity of the acceptor and donor molecules, respectively, after excitation of the donor. These experiments yielded more accurate values for the distance between donor and acceptor molecules, and hence, spFRET became a useful spectroscopic ruler for analyzing the distances of interaction between biomolecules. Despite the improvement over bulk FRET measurements, spFRET still had problems associated with the heterogeneity of the population of labeled molecules. For example, incomplete labeling, fluorescent dye photophysics, and photobleaching can all lead to an apparently low FRET efficiency, but none of these are representative of the actual interaction of interest. Furthermore, spFRET did not provide a general platform for quantitative analysis of molecular interactions, i.e., the stoichiometry of interactions. This is because spFRET does not take into account whether there is more than one donor and/or acceptor molecule present in the interaction. These shortcomings were overcome with the introduction of alternating laser excitation FRET, first developed by Kapanidis et al.

[38,39]. In this scheme, the donor and acceptor molecules are alternately excited by the donor excitation laser and the acceptor excitation, respectively. The fluorescence emission intensities from the donor and acceptor molecules after donor excitation are still used in determining E . However, the direct acceptor excitation and subsequent emission is used as verification of the presence of an actual FRET pair. Additionally, it can now be used as part of a new ratiometric calculation that provides information on the stoichiometry of donor–acceptor molecules. This ratio, which was first defined by Kapanidis, was termed, S , for stoichiometric ratio, and is given as follows:

$$S = \frac{F_{D_{ex}}}{F_{D_{ex}} + F_{A_{ex}}}, \quad (4.38)$$

where $F_{D_{ex}}$ is the combined donor and acceptor fluorescence after donor excitation and $F_{A_{ex}}$ is the acceptor fluorescence after direct acceptor excitation. A sample with no acceptor molecule present would therefore yield an S value of 1, and conversely, a sample with no donor molecule would yield an S value of 0. For different ratios of donor to acceptor, S ranges between 0 and 1. Because the expression for S depends on both the donor and acceptor excitation wavelengths, the value obtained for a given donor to acceptor ratio will depend on the ratio of excitation laser intensities, i.e., on I_d/I_a , where $I_{d,a}$ are the intensities of the donor and acceptor laser intensities. Kapanidis et al. [40] showed that the best discrimination between different S values is obtained when S is set at 0.5 for a 1:1 donor-to-acceptor ratio. By coupling these two quantities, E and S , into a 2D distribution, we can further separate out populations of complexes based on their interaction distance and stoichiometry information (see Figs. 4.23 and 4.24). A simple electronic delay line is inserted to delay the triggering of donor laser excitation pulses with respect to the acceptor laser excitation pulses. This type of excitation has been termed pulsed interleaved excitation FRET, or PIE FRET [41]. An initial study using double-stranded DNA constructs has been designed with one donor, Alexa488, and one acceptor, Alexa647, at varying distances, starting from directly across on the duplex, and then in steps of 5 base pairs away, and to a maximum distance of 20 base pairs. The geometry of the donor–acceptor distances is shown in Figure 4.25a; donor emission and acceptor fluorescence spectra are shown in Figure 4.25b.

The PIE mode allows for discrimination against complexes lacking donor or acceptor molecules. FRET efficiency was calculated using the following expression:

$$E = \frac{F_{D_{ex}}^{A_{em}}}{F_{D_{ex}}^{A_{em}} + \gamma F_{D_{ex}}^{D_{em}}}, \quad (4.39a)$$

$$\gamma = \frac{\phi_A \eta_A}{\phi_D \eta_D}, \quad (4.39b)$$

where $F_{D_{ex}}^{A_{em}}$ is the acceptor emission after donor excitation, i.e., FRET fluorescence, and $F_{D_{ex}}^{D_{em}}$ is the donor emission after donor excitation; γ is the relative efficiency factor, which takes into

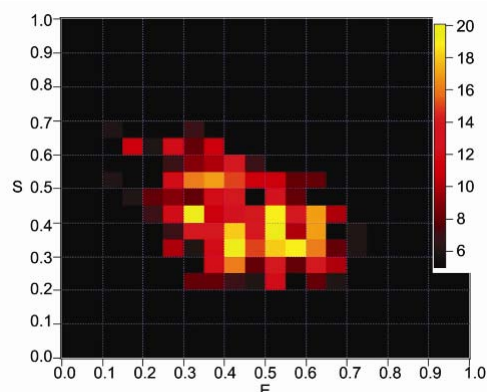


Figure 4.23. Example of a two-dimensional E-S histogram obtained with pulsed interleaved excitation FRET data acquisition. E is the energy transfer efficiency, and ranges from 0 to 1. S is defined as the stoichiometric ratio, and it depends on the ratio of donor to acceptor molecules present in a FRET complex. It also ranges from 0 to 1. Thus, populations of single complexes can be rapidly separated using their coupled E and S values. Please visit <http://www.springer.com/series/7845> to view a high-resolution full-color version of this illustration.

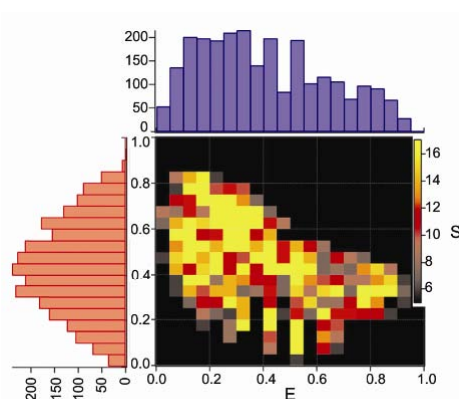


Figure 4.24. ES distribution for sample with 2 donors and 2 acceptors. Both 2D ES and 1D S distributions illustrate the complication of subpopulation convolution on the overall distribution of S values. It becomes difficult to ascertain which populations are actually present, and furthermore, no distinction can be made between a donor-acceptor pair with a ratio of 1:1 or 2:2 in terms of their calculated S values. Please visit <http://www.springer.com/series/7845> to view a high-resolution full-color version of this illustration.

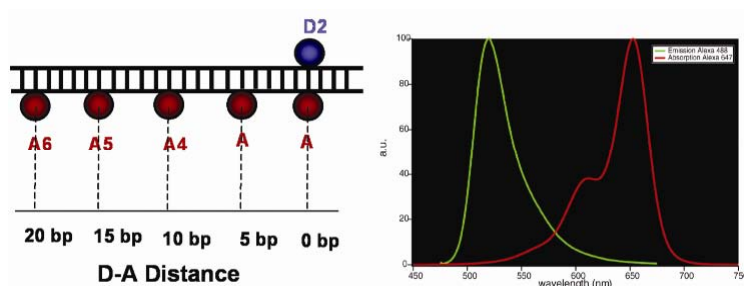


Figure 4.25. (a) Diagram of donor-acceptor distances in base pairs on DNA duplex constructs. (b) The Alexa Fluor 488 donor emission and Alexa Fluor 647 acceptor absorption. Please visit <http://www.springer.com/series/7845> to view a high-resolution full-color version of this illustration.

account the difference in quantum yield, ϕ , and detection efficiency, η , for the donor and acceptor dyes. For the specific FRET pair used in this study, $\gamma \sim 1$. the efficiency calculated for this test system is shown in Table 4.1.

Table 4.1. Summary of FRET Efficiency Values Obtained for Single Complexes on the Surface of a Microscope Coverslip

D-A in base pairs	FRET E	Std. dev.
0	0.72	0.03
5	0.68	0.05
10	0.48	0.04
15	0.39	0.04
20	0.34	0.06

Sample geometry and sequence are shown in Figure 4.25.

4.6. DYNAMIC PROCESSES PROBED BY FLUORESCENCE

4.6.1. Fluorescence Recovery after Photobleaching (FRAP)

The presence of photobleaching is almost inevitable in any of the fluorescence spectroscopy measurements. The process of *isc* exists in some capacity for all systems. In the previous section we discussed approaches used to minimize the effects of photobleaching. We now discuss how investigators have devised methods to take advantage of the omnipresence of this problem. One very successful way of handling the photobleaching problem is to design an experiment that probes the dynamics of fluorophores after a part of the population was photobleached beforehand. This process is called Fluorescence Recovery after Photobleaching or (FRAP).

The essence of this process is to first controllably deplete the fluorophores of a dynamic population of molecules. Then a probing signal follows to monitor the return of fluorophore-laden molecules to the same bleached-out spatial region. The initial research using FRAP was conducted on membrane systems, where the photobleached membrane fluorophores exchange with non-photobleached fluorophores via a 2D random diffusion process. The return of the intensity of fluorophores within the bleached-out region is exponential, and the $1/e$ time (Fig. 4.26) relates to 2D translational diffusion. This method became established as a sure way to measure the dynamics of molecules.

An extension of this method to probing orientational dynamics has also been established. In such an experiment a well-defined polarization of exciting light can be used to photobleach out a specific polarization of fluorophores. By monitoring the polarization population's return to its original intensity, a rotational diffusion coefficient is measured. An up-to-date review of the theory of this process is presented by Wolf [42].

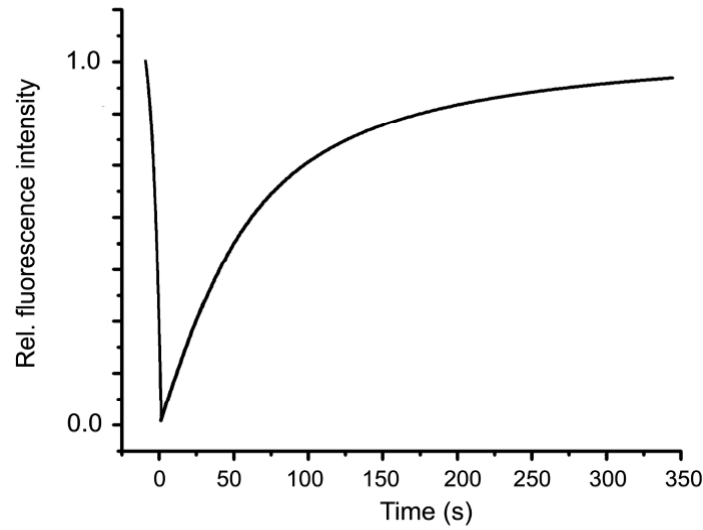


Figure 4.26. FRAP experiment. Recovery of fluorescence after an initial photobleaching pulse within the same sampled domain (volume or area) is due to dynamic movement of non-bleached fluorophores into the bleached region. Time of recovery is related to dynamic driving forces on the fluorophores.

4.6.2. Fluorescence Correlation Spectroscopy (FCS)

One of the most useful methods for obtaining dynamic information on fluorescent systems is by measurement of the spontaneous change of the fluctuating intensity of fluorophores by measuring the pairwise time correlation function of the fluorophore's intensity. The basic theory of the degree of second-order coherence of light, is given by [4]

$$g^{(2)}(\tau) = \frac{\langle I(\tau)I(t+\tau) \rangle}{\langle I \rangle^2} = \frac{\langle E^*(t)E^*(t+\tau)E(t+\tau)E(t) \rangle}{\langle E^*(t)E(t) \rangle^2}, \quad (4.40)$$

where the angular brackets indicate averages over long times. For a classical light source, such as emission from a mercury lamp, $g^{(2)}(\tau)$ has the following features:

$$g^{(2)}(-\tau) = g^{(2)}(\tau), \quad (4.41a)$$

$$g^{(2)}(0) \geq 1, \quad (4.41b)$$

$$g^{(2)}(\tau) \leq g^{(2)}(0). \quad (4.41c)$$

For a system of interacting and freely diffusing fluorescent molecules in a small detection volume, the fluctuations in intensity are due to the fluctuations in the concentration, or number, of molecules in this volume (see [43–45]). These changes in concentration are directly the result of diffusion of molecules into and out of the detection volume and the chemical reaction kinetics (see Fig. 4.27).

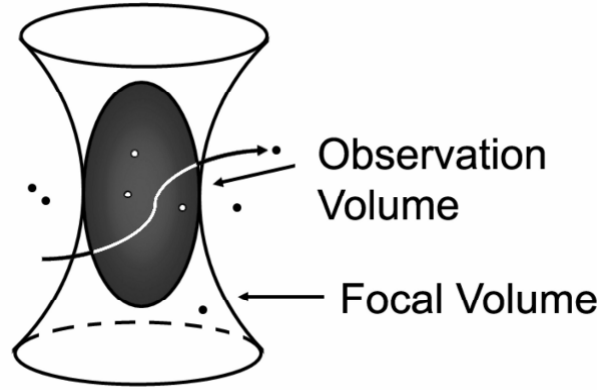


Figure 4.27. Description of observation volume. Molecules are excited as they diffuse into the confocal volume, and the detection volume is limited to, in theory, an ellipsoidal volume with lateral and axial diameters given by the optical limit of resolution.

Stating this mathematically, the changes in fluorescence emission are proportional to the changes in concentration [46]:

$$\delta F(\mathbf{r}, t) = \phi(\mathbf{r}) \delta N(\mathbf{r}, t) = \phi(\mathbf{r}) \delta C(\mathbf{r}, t) d\mathbf{r}, \quad (4.42)$$

where $\phi(\mathbf{r})$ is the detectability, is a function of position \mathbf{r} , and is determined by the optical system used to define the detection volume. The temporal autocorrelation of the fluorescence intensity fluctuations thus yields the timescale of the above-mentioned dynamics as well as the average number of molecules $\langle N \rangle$ in the probe volume. Mathematically, the autocorrelation, $G(\tau)$, of these fluorescence intensity fluctuations, $\delta F(t)$, is calculated as the time average of the product of the fluctuations at every time t and the fluctuations at delay times $t + \tau$ (see Fig. 4.28). Normalization of this function is by the squared time average of the fluorescence emission, $F(t)$:

$$G(\tau) = \frac{\langle \delta F(t) \delta F(t + \tau) \rangle}{\langle F(t) \rangle^2}. \quad (4.43)$$

Using the relationship between the concentration and fluorescence intensity given in Eq. (4.29), $G(\tau)$ can be expressed as [46]

$$G(\tau) = \frac{\int \int \phi(\mathbf{r}) \phi(\mathbf{r}') \langle \delta C(\mathbf{r}, t + \tau) \delta C(\mathbf{r}', t) \rangle d\mathbf{r} d\mathbf{r}'}{\langle C \rangle^2 \left[\int \phi(\mathbf{r}'') d\mathbf{r}'' \right]^2} \quad (4.44)$$

To calculate the above expression for $G(\tau)$, it is necessary to solve for the concentration fluctuations with respect to time given the dynamical process contributing to the changes in

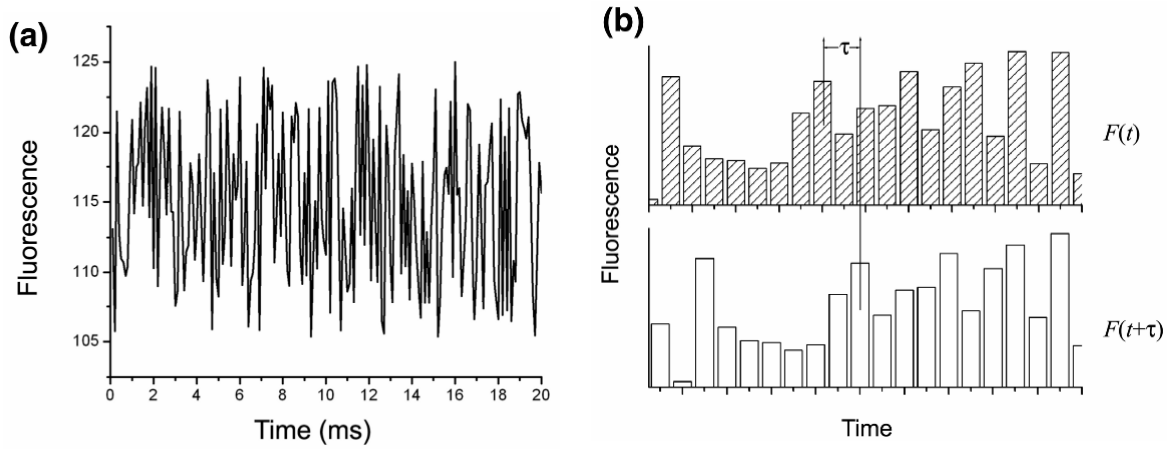


Figure 4.28. Example of fluorescence intensity fluctuations versus time, shown in (a). The fluorescence intensity traces shown in (b) illustrate the calculation of the correlation as a product of the fluorescence fluctuations at every time and the corresponding fluctuations at delay times $t + \tau$.

concentration, i.e., those of diffusion and chemical kinetics. For a system of chemically interacting species, j , in equilibrium, the rate of changes in concentration fluctuations is given by the following differential equation [43]:

$$\frac{\partial \delta C_j(\mathbf{r}, t)}{\partial t} = D_j \nabla^2 \delta C_j(\mathbf{r}, t) + \sum_k T_{jk} \delta C_k, \quad (4.45)$$

where D_j is the three-dimensional diffusion coefficient for species j , and T_{jk} are the elements of the matrix of linear chemical interaction coefficients implied by the following reaction:



The equilibrium constant is given by

$$K = \frac{k_f}{k_b} = \frac{\bar{C}_C}{\bar{C}_A + \bar{C}_B}, \quad (4.47)$$

where the equilibrium concentrations of A , B , and C are given by \bar{C}_A , \bar{C}_B , \bar{C}_C . Assuming the idealized detection volume described above, $\phi(\mathbf{r})$ is a three-dimensional Gaussian function, with half-axes of r and l . For the simplest case of only one species and no chemical kinetics, $G(\tau)$ is given by [46]

$$G(\tau) = \left(\frac{1}{N} \right) \left(\frac{1}{1 + \frac{4D\tau}{r^2}} \right) \left(\frac{1}{1 + \frac{4D\tau}{l^2}} \right)^{\frac{1}{2}}. \quad (4.48)$$

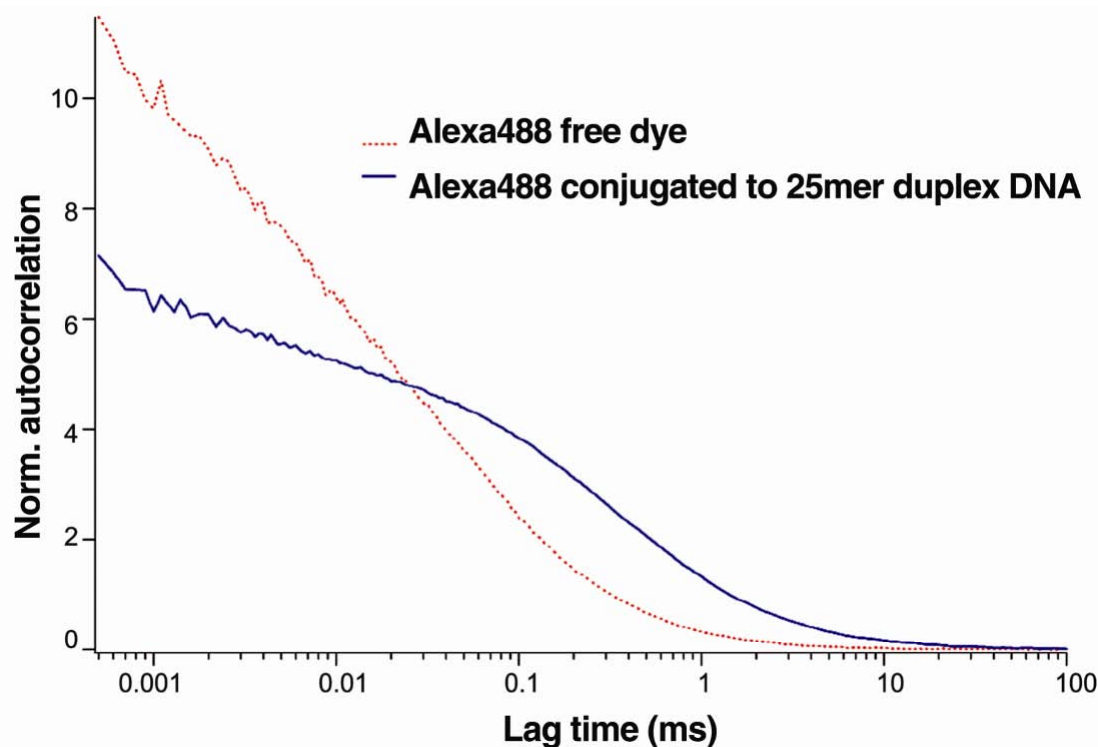


Figure 4.29. Comparison of the FCS autocorrelation calculation of Alexa Fluor 488 dye alone (red curve) and conjugated to a 25-base pair DNA duplex (blue curve). Free dye exhibits shorter diffusion times compared to dye conjugated to a larger DNA duplex molecule. Please visit <http://www.springer.com/series/7845> to view a high-resolution full-color version of this illustration.

Although this expression represents a highly idealized situation, it was derived in order to illustrate the key features of FCS and its applicability to studying interacting species of molecules. Recently, theoretical and experimental analyses have been presented to characterize the effect of experimental artifacts on the measurement of $G(\tau)$ [47,48]. Two examples of FCS traces are shown in Figure 4.29. The plot clearly indicates two different diffusion times. The faster one corresponds to free Alexa488 dye in buffer solution, and the slower one corresponds to Alexa488-labeled 25mer duplex DNA in the same buffer. This example nicely illustrates the sensitivity of FCS to diffusion dynamics. One other useful parameter that can be extracted from the above results is the average number of molecules in the detection volume, $\langle N \rangle$ [46]. From Eqs. (4.3) and (4.5) one obtains $G(0) = 1/\langle N \rangle$, assuming that $\phi(\mathbf{r})$ is a smooth function of \mathbf{r} . Since the effective volume $\langle V \rangle$ is given by

$$\langle V \rangle = \frac{\langle N \rangle}{\langle C \rangle}, \quad (4.49)$$

and

$$G(0) = \frac{1}{[\langle C \rangle \langle V \rangle]}. \quad (4.50)$$

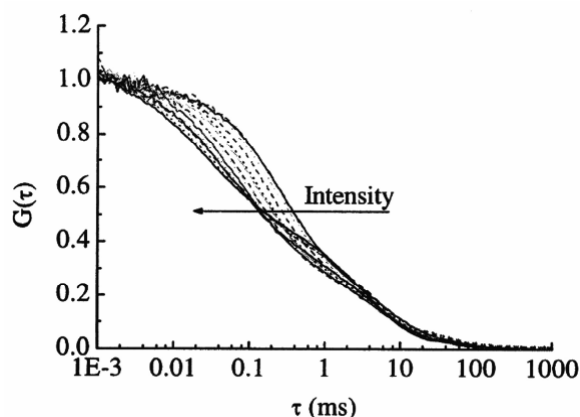


Figure 4.30. Fluorescence correlation function profile: $G(\tau)$ vs. $\ln \tau$. The $\frac{1}{2}G(\tau)$ point represents the lifetime τ_r of the species under investigation. Reactions alter the correlation function as shown, by changing the position of τ_r . This could be due to diffusional and reactive dynamics.

FCS can be extended to study reactive species if one of the reactants or the product is fluorescent (see Fig. 4.30). In an example of using FCS to monitor chemical reaction, we consider the protonation reaction associated with EGFP [49].

4.6.3. Antibunching Spectroscopy

A particularly intriguing aspect of fluorescence correlation spectroscopy develops if the number of fluorophores being sampled is very small. In that case, it can be shown that, given the lifetime of the fluorophore is τ , when FCS is conducted on systems over times short compared to the lifetime, the probability of finding a correlated emission is very low. Indeed, it is precisely 0 for $g^{(2)}(0)$. This phenomenon is thus called “antibunching.” It reflects the fact that if sampling is done in time prior to the full lifetime of the fluorophore, there will not be any emission, so that the correlation is vanishingly small. The expression is given here:

$$g^{(2)}(t) = \frac{N(N-1)}{N^2} + \frac{1}{N} \left(1 - e^{-\frac{t}{\tau}} \right). \quad (4.51)$$

We can see for the emission from single fluorescent dyes that

$$g^{(2)}(0) = 1 - \frac{1}{N} < 1, \quad (4.52)$$

as expected for antibunched light. The above expression for the intensity correlation function is only dependent on the number of molecules present, N , and the excited state lifetime, τ . Thus $g^{(2)}(t) < 1$ for $t \ll \tau$, which increases to 1 at a rate that is determined by the excited-state lifetime. Such a measurement on a system of independent quantum emitters yields N and τ , two parameters that can provide useful information with respect to interacting biological systems. An example of such a measurement is shown in Figure 4.31 [50].

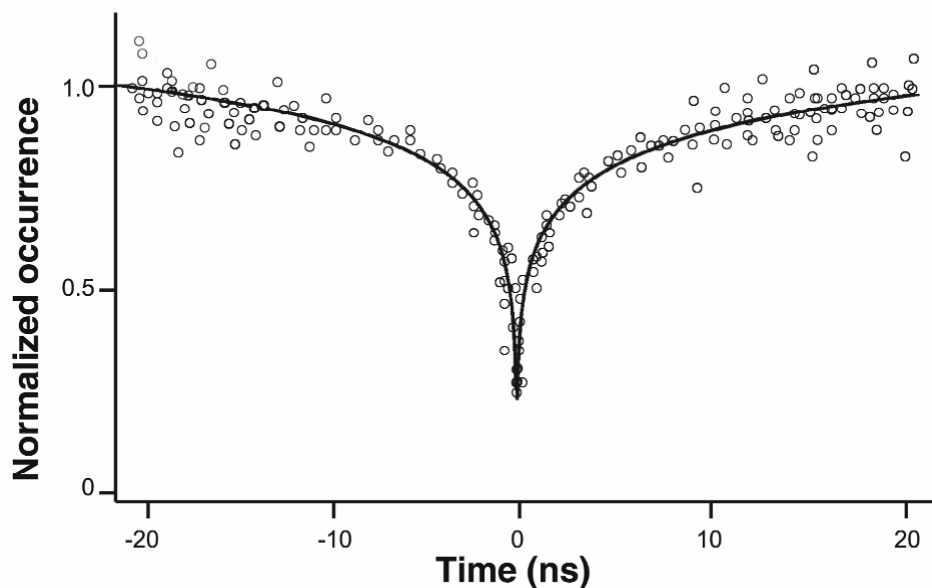


Figure 4.31. Time-correlated single-photon counting measurement of the emission from single Rhodamine 6G molecules detected by single-photon counting photodetectors in a Hanbury Brown Twiss (HBT) interferometer. The probability of detecting simultaneous photon events is zero for a single R6G molecule. Background emission creates a measurement of $g^{(2)}(0)$ greater than zero. Negative times are introduced by time delaying one of the detectors in the HBT interferometer with respect to the other.

The above expression is valid for continuous-wave laser excitation. This is because at any time t , assuming the molecule is in the ground state, it can absorb a photon. Using pulsed excitation, the times at which a molecule can absorb a photon are dependent on when the laser is pulsing. In this situation, photon pairs can only have a time difference that is a multiple of the laser repetition rate. A comparison of the results for the two modes of excitation is shown in Figure 4.32. For pulsed excitation mode, N can be determined by comparing the area of the peak at zero time delay, that is, coincident photon pairs, to the average area of the noncoincident adjacent peaks:

$$\frac{g^{(2)}(0)}{g^{(2)}(\infty)} = 1 - \frac{1}{N}, \quad (4.53)$$

due to the normality condition of $g^{(2)}(t)$, and the nature of antibunched light. For repetition rates much longer than the excited state lifetime, $g^{(2)}(t) \approx g^{(2)}(\infty)$. Thus experimentally, the area ratio of the coincident peak to noncoincident peak average is equivalent to $1 - 1/N$ [51].

4.6.4. Coupling of FRET or PET to FCS

One of the most powerful methods of obtaining dynamic information from molecular groups at very small distances is a combination of the high-spatial resolution FRET method with the temporal method of FCS. If the FRET pair exhibits an acceptor signal due to its proximity to the

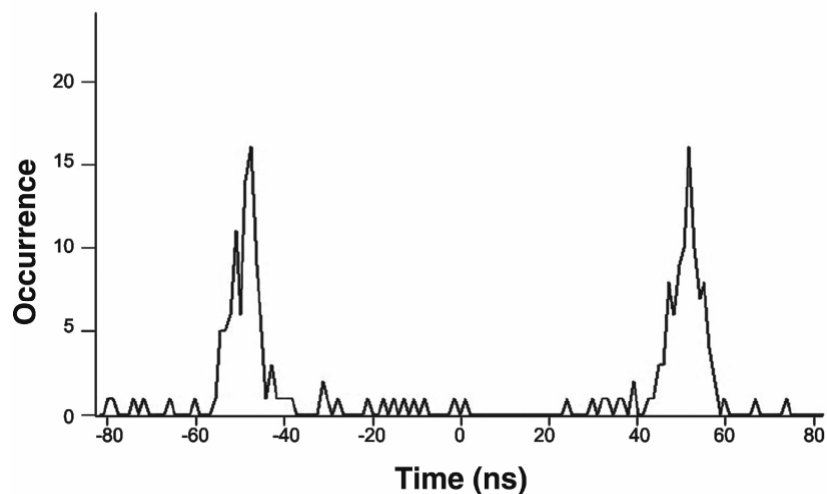


Figure 4.32. Pulsed antibunching data showing zero signal at coincidence time $\tau = 0$. Data indicate that the $G(\tau)$ vs. τ are derived from a single fluorophore, thus providing a means to quantitate single-molecular events.

donor, and the approach to proximity is a dynamic process, such as a biochemical reaction, conducting a FRET-FCS experiment provides information about the rate process associated with the presence of the FRET signal. Note that the FRET-FCS signal provides a much tighter spatial localization than offered by a two-color fluorescence colocalization experiment because, due to the point-spread function (PSF), a colocalized signal is only as good as 200 nm. Since the FRET signal measures distances more on the molecular range, <20 nm, dynamic monitoring of such a signal provides detailed information about intramolecular or intermolecular reactions often involved in molecular folding or enzyme binding. The key criterion is to ensure that the process to be investigated is not being compromised by the presence of the fluorophore [41].

Sauer et al. have shown that certain dyes — including Alexa488 — in the presence of protein residue Trp or nucleic acid G will elicit photoinduced electron transfer. This process is even shorter ranged than those sampled by FRET. Here there is a <2 nm distance sampling [28].

FRET can also be coupled with special FCS sampling at very short times to achieve FRET-antibunching FCS. In such a situation the FRET signal is seen to provide stoichiometric information on FRET pairs.

4.6.5. Total Internal Reflection Fluorescence (TIRF) and Imaging FCS

Given the tools mentioned in this chapter, it is tempting to explore the possible use of all of them in an effort to study fluorophore-labeled intracellular molecules as the signal is being produced due to intracellular molecular processes. What is needed is not point sampling but a larger spatial domain, so that imaging is required. However, most imaging processes do not have spatial resolution capability. In order to deal with lateral resolution, the FRET signal or the PET signal will suffice. In the z -plane, however, the approach employed will be to use total internal reflection-driven fluorescence, or TIRF. By combining image capture in time and TIRF, z -

sampling will also be able to limit the contributing signals that arise from the $1/e$ fold of the exciting TIR signal, which is typically <100 nm.

Having the image is one important step. However, the more critical step is to obtain dynamic information on how these fluorophores or fluorophore-laden molecules are moving on the cell surface or intracellularly. This leads to the need for combining TIRF imaging capability, which allows successive capture of images in time, with the ability to perform one of two experiments: image FCS [52,53] or particle tracking dynamics.

4.6.5.a. Image FCS

In this mode of measuring the dynamics of captured features, the spatial positions of each emitting fluorophore is captured and stored. Since information about particular events captured may be spatially or temporally significant, the image FCS (I-FCS) method can perform either mode of information retrieval. If the significant feature is to examine the spatial distribution of a set of emitting fluorophores, then a two-point spatial correlation value is computed for every captured feature within a single timeframe (captured image). This leads to a spatial distribution function plot, which usually can reveal aggregation phenomena or periodic structures within the image [54]. If the significant feature is in the temporal feature of a specifically identified set of fluorophores, then a temporal I-FCS is computed [55]. A generalized I-FCS function that is a function of spatial lag variables ζ and η , and of a temporal lag variable τ , is defined as

$$g_i(\zeta, \eta; \tau) = \frac{\langle (i(x, y; t) - \langle i(x, y; t) \rangle)(i(x + \zeta, y + \eta; t + \tau) - \langle i(x, y; t + \tau) \rangle) \rangle}{\langle i(x, y; t) \rangle \langle i(x, y; t + \tau) \rangle}. \quad (4.54)$$

The analytical expressions of spatial and temporal features are given below:

1. *Distribution analysis by spatial I-FCS.* For fluorophores on a surface perpendicular to a Gaussian laser beam at its focal point, the autocorrelation function ($\tau = 0$) decays as a Gaussian:

$$g_i(\zeta, \eta; 0) = g_i(0, 0; 0)e^{-(\zeta^2 + \eta^2)/w^2} + g_0, \quad (4.55)$$

where w^2 is the square of the widths of the laser beam. Gaussian fitting of the autocorrelation function yields a value of $g_i(0, 0; 0)$, which can be used to quantify the distribution of those fluorophores in terms of Cluster Density(CD), average occupation number \bar{N}_p , and Degree of Aggregation (DA):

$$CD_i = \frac{\bar{N}_p}{\pi w^2} = \frac{1}{g_i(0, 0; 0)\pi w^2}, \quad (4.56)$$

$$DA_i = g_i(0, 0; 0) \langle i(x, y, t) \rangle. \quad (4.57)$$

2. *Dynamic analysis by temporal I-FCS.* The image cross-correlation function with time lag τ can reveal the rate of dynamic changes in the image sequence. If the spatial distribution fluctuates because of the diffusion of components in the plane of the image, the I-FCS function remains Gaussian, but it is modulated by a diffusive component:

$$g_{ij}(\zeta, \eta; \tau) = g_{ij}(0, 0; 0) \exp \left[\frac{-(\zeta^2 + \eta^2)/w^2}{1 + \tau/\tau_d} \right] [1 + \tau/\tau_d]^{-1}. \quad (4.58)$$

Obviously, the peak of I-FCS function amplitude $g_{ij}(0, 0; \tau)$ decays as

$$g_{ij}(0, 0; \tau) = g_{ij}(0, 0; 0) [1 + \tau/\tau_d]^{-1}, \quad (4.59)$$

One can then calculate the diffusion characteristic time τ_d and then the diffusion coefficient:

$$D = w^2 / 4\tau_d. \quad (4.60)$$

An illustration of the versatility of this method, applied in quantitative studies of lipid raft distribution and dynamics [56], is provided in Figure 4.33a,b.

4.6.5.b. Particle Tracking Dynamics

Realizing that having obtained a two-point, space-time correlation function is NOT the entire story of a specific molecular system, a more complete approach is to obtain the full movement features of the specifically identified fluorophores, in space and time. This approach allows for the full distribution function of the particle, in space and time, to be obtained. Such a method is called particle tracking. It has been very successfully implemented in a number of situations, including those related to membrane dynamics and others associated with the dynamic movements of myosin or kinesin motors. A special chapter in this volume is devoted to this approach of obtaining useful information about the dynamics of molecules, particularly for intracellular events.

4.6.6. Zero-Mode Waveguide Structures in Fluorescence Spectroscopy

One of the requirements in conducting single-molecule fluorescence spectroscopy is that the samples have to be truly sparse so that single-molecule events can be individually tracked and monitored. This usually amounts to saying that within the optically sampled volume, $500 \times 500 \times 1000 \text{ nm}^3 = 2.5 \times 10^{-18}$ liters, one molecule is being detected at a time. Applying the general rule of focal volume confinement using a high-NA lens, this leads to a solution molar concentration of $<1 \text{ nM}$. In an experiment conducted in vitro, this is not a problem. However, should one be required to mimic a biochemical reaction, monitoring its activity in a realistic environment, this is often too low of a value. A solution with less than that called for by the equilibrium constant, K , will cause a back reaction to increase the solution concentration. So one way to artificially limit the sampling volume is to put up artificial nano-barriers. The zero-mode waveguide concept, advanced by Levene et al. [57], promotes fabricated nano-structures with open holes $\sim 50 \text{ nm}$ in dimension within a thin metal deposition on a transparent substrate. This dimension is too small for an electromagnetic wave to propagate through. Hence what is within these openings is the evanescent wave decaying within 100 nm . Effectively, one has set up a construct where the dimension for optical illumination is now at $50 \times 50 \times 100 \text{ nm}^3 = 2.5 \times 10^{-21}$ liters! This dimension is approximately 1000 times smaller than the open focal volume. Thus a

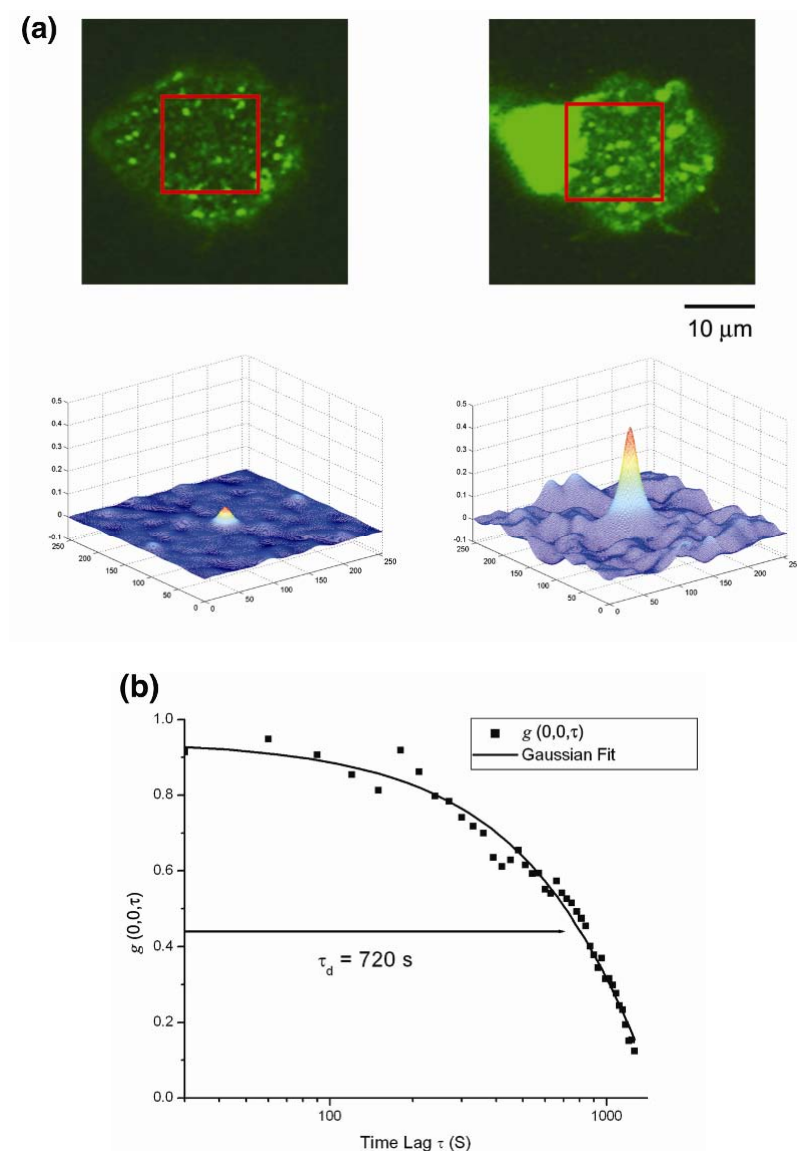


Figure 4.33. (a) Fluorescent microscopic images of healthy (*left*) and apoptotic (*right*) human retinal pigment epithelial (RPE) cells, labeled with BODIPY-FL-Gm1, and their autocorrelation functions (spatial I-FCS) of cropped areas. The autocorrelation function's peak height and width quantify the distribution of green fluorophores (labels for lipid rafts) in terms of Cluster Density (CD) and Degree of Aggregation (DA). (b) Cross-correlation (temporal I-FCS) function $g_{ij}(0,0,\tau)$ computed from a sequence of images of healthy RPE cells, taken every 30 seconds. Diffusion characteristic time τ_d , the time when $g_{ij}(0,0,\tau) = g_{ij}(0,0,0)/2$, quantifies diffusion coefficient. $D = w^2/(4\tau_d) = 0.03 \mu\text{m}^2/\text{s}$. Please visit <http://www.springer.com/series/7845> to view a high-resolution full-color version of this illustration.

single molecule sampled within this volume could be from a reaction with an equilibrium constant 1000 times larger than the open system. Micromolar concentrations are much easier to deal with because many biochemical reactions will have such values of the constant K .

A sample of such a device is shown in Figure 4.34a, where an illustration of the ability to sample biochemical reaction is given, while Figure 4.34b shows FCS traces for samples at micromolar concentrations collected within this ZMW structure. Work expanding on the versatility of this structure has been recently published [41].

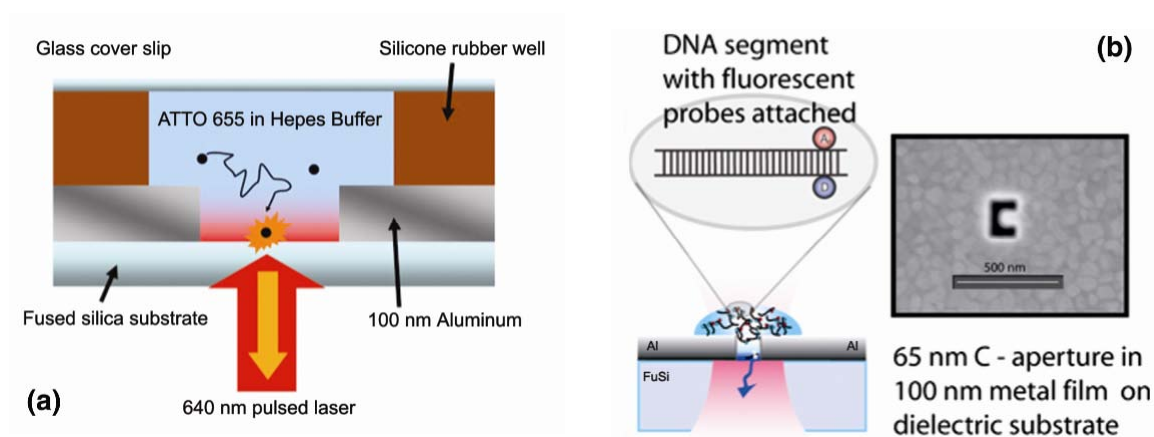


Figure 4.34. (a) Concept of a zero-mode waveguide-illuminated fluorescence event. Construct limits propagation of light into the small nanoaperture, leading to evanescent wave propagation. (b) Special nanoaperture is shaped in the form of the letter “C.” This structure (at nano dimension) leads to plasma resonance reinforcement of an evanescent wave within the cavity, allowing for single-molecule excitation and subsequent studies. Reprinted with permission from [41]. Copyright © 2007, IOP Publishers. Please visit <http://www.springer.com/series/7845> to view a high-resolution full-color version of this illustration.

ACKNOWLEDGMENTS

This work is supported in part by The Center for Biophotonics, a National Science Foundation Science and Technology Center managed by the University of California, Davis, under Cooperative Agreement No. PHY 0120999. The authors are greatly appreciative of the contributions of Professor Thomas Huser.

PROBLEMS

- 4.1.
 - a. Estimate the spatial optical resolution of a fluorescent microscope with a $100\times$ 1.45-NA objective lens, if the excitation source is a 488-nm laser.
 - b. Lambda DNA isolated from lambda phage (*Enterobacteria phage λ*) has 48,502 base pairs. It is about $16\text{ }\mu\text{m}$ long when fully extended. However, the DNA is only 20 nm wide, far below the optical resolution. Explain why this DNA can be visualized in the fluorescent microscope, when it is labeled with YOYO. (Hint: viewing holiday lights from a great distance.)

- 4.2. A photomultiplier tube (PMT) is used in an FCS setup to count photon numbers. Below are depicted two records from the PMT for two samples. However, both the time (x-axis) and intensity (y-axis) values are missing. Based on the graphic information, which sample has a higher concentration of fluorophores? Explain your answer.



Sample 1



Sample 2

- 4.3. Suppose that a protein is genetically fused with two fluorescent proteins, CFP and YFP, at its two terminals. When activated, the protein will switch from bend conformation to extended conformation. This system is excited by a 436-nm laser. Two PMTs are recording the CFP channel (488 nm) and the YFP channel (528 nm). The efficiency of the energy transfer is expressed as $E = I_{528}/(I_{488} + I_{528})$. Most of the time the value of E is 0.7, but there are short periods of time when it drops to 0.1. Assuming that the Förster distance (R_0) for CFP and YFP is about 5 nm, estimate how far this protein is extended when activated.

REFERENCES

1. Lakowicz JR. 2006. *Principles of fluorescence spectroscopy*, 3rd ed. New York: Springer. 954.
2. Jackson JD. 1999. *Classical electrodynamics*, 3rd ed., New York: Wiley.
3. Loudon R. 2000. *The quantum theory of light*, 3rd ed. Oxford: Oxford UP.
4. Loudon R. 2000. *The quantum theory of light*, 3rd ed. New York: Oxford UP.
5. Cantor CR, Schimmel PR. 1980. *Biophysical chemistry*. San Francisco: W.H. Freeman.
6. Turro NJ. 1991. *Modern molecular photochemistry*. Mill Valley, CA: University Science Books.
7. Stokes GG. 1852. On the change of refrangibility of light. *Phil Trans R Soc (London)* **142**:463–562.
8. Pedrotti FL, Pedrotti LS, Pedrotti LM. 2007. *Introduction to optics*, 3rd ed. Upper Saddle River, NJ: Pearson Prentice-Hall.
9. So PTC, Dong CY, Masters BR, Berland KM. 2000. Two-photon excitation fluorescence microscopy. *Ann Rev Biomed Eng* **2**:399–429.
10. Yazdanfar S, Chen YY, So PTC, Laiho LH. 2007. Multifunctional imaging of endogenous contrast by simultaneous nonlinear and optical coherence microscopy of thick tissues. *Microsc Res Tech* **70**(7):628–633.
11. Niggli E, Egger M. 2004. Applications of multiphoton microscopy in cell physiology. *Front Biosci* **9**:1598–1610.

12. Prasad PN. 2003. *Introduction to biophotonics*. Hoboken: John Wiley & Sons.
13. Denk W, Piston D, Webb W. 1995. Two-photon molecular excitation in laser scanning microscopy. In *Handbook of biological confocal microscopy*, 2nd ed., pp. 445–458. Ed. JB Pawley. New York: Plenum Press.
14. Axelrod D. 1989. total internal-reflection fluorescence microscopy. *Methods Cell Biol* **30**:245–270.
15. Evanescent Wave Imaging Systems Brochure, 2006. Nikon.
16. Burghardt TP, Ajtai K, Borejdo J. 2006. In situ single-molecule imaging with attoliter detection using objective total internal reflection confocal microscopy. *Biochemistry* **45**(13):4058–4068.
17. Ajtai K, Peyser YM, Park S, Burghardt TP, Muhlrad A. 1999. Trinitrophenylated reactive lysine residue in myosin detects lever arm movement during the consecutive steps of ATP hydrolysis. *Biochemistry* **38**(20):6428–6440.
18. Fitzgerald JT, Michalopoulou A, Pivetti CD, Raman RN, Troppmann C, Demos SG. 2005. Real-time assessment of in vivo renal ischemia using laser autofluorescence imaging. *J Biomed Opt* **10**(4):44018.
19. Clark AP, Longfellow DG, Seifried HE. 1993. Benzo[a]pyrene. In *Handbook of analytical and spectral data for polycyclic aromatic hydrocarbons*, Vol. 1: *Benzo[a]pyrene and its metabolites*, pp. 5–10. Ed DG Longfellow. Kansas City: Midwest Research Institute.
20. Cosman M, de los Santos C, Fiala R, Hingerty BE, Singh SB, Ibanez V, Margulis LA, Live D, Geacintov NE, Broyde S, Patel DJ. 1992. Solution conformation of the major adduct between the carcinogen (+)-anti-benzo[a]pyrene diol epoxide and DNA. *Proc Natl Acad Sci USA* **89**(5):1914–1918.
21. Eggleston AK, Rahim NA, Kowalczykowski SC. 1996. A helicase assay based on the displacement of fluorescent, nucleic acid-binding ligands. *Nucleic Acids Res* **24**(7):1179–1186.
22. Tsien RY. 1998. The green fluorescent protein. *Annu Rev Biochem* **67**:509–544.
23. Niwa H, Inouye S, Hirano T, Matsuno T, Kojima S, Kubota M, Ohashi M, Tsuji FI. 1996. Chemical nature of the light emitter of the *Aequorea* green fluorescent protein. *Proc Natl Acad Sci USA* **93**(24):13617–13622.
24. Fischer AJ, Lagarias JC. 2004. Harnessing phytochrome's glowing potential. *Proc Natl Acad Sci USA* **101**(50):17334–17339.
25. Bianco PR, Brewer LR, Corzett M, Balhorn R, Yeh Y, Kowalczykowski SC, Baskin RJ. 2001. Processive translocation and DNA unwinding by individual RecBCD enzyme molecules. *Nature* **409**(6818):374–378.
26. Spies M, Bianco PR, Dillingham MS, Handa N, Baskin RJ, Kowalczykowski SC. 2003. A molecular throttle: the recombination hotspot chi controls DNA translocation by the RecBCD helicase. *Cell* **114**(5):647–654.
27. Sauer M. 2005. Reversible molecular photoswitches: a key technology for nanoscience and fluorescence imaging. *Proc Natl Acad Sci USA* **102**(27):9433–9434.
28. Heinlein T, Biebricher A, Schluter P, Roth CM, Herten DP, Wolfrum J, Heilemann M, Muller C, Tinnefeld P, Sauer M. 2005. High-resolution colocalization of single molecules within the resolution gap of far-field microscopy. *Chemphyschem* **6**(5):949–955.
29. Weber G. 1952. Polarization of the fluorescence of macromolecules, 2: fluorescent conjugates of ovalbumin and bovine serum albumin. *Biochem J* **51**(2):155–168.
30. Weber G. 1952. Polarization of the fluorescence of macromolecules, 1: theory and experimental method. *Biochem J* **51**(2):145–155.
31. Cherry RJ, Cogoli A, Oppliger M, Schneider G, Semenza G. 1976. A spectroscopic technique for measuring slow rotational diffusion of macromolecules, 1: preparation and properties of a triplet probe. *Biochemistry* **15**(17):3653–3656.
32. Axelrod D, Koppel DE, Schlessinger J, Elson E, Webb WW. 1976. Mobility measurement by analysis of fluorescence photobleaching recovery kinetics. *Biophys J* **16**(9):1055–1069.
33. Förster T. 1948. Intermolecular energy migration and fluorescence. *Ann Phys* **2**:55–75.
34. Cantor CR, Schimmel PR. 1980. *Biophysical chemistry: techniques for the study of biological structure and function*, Vol. 2. San Francisco: W.H. Freeman.
35. Gordon GW, Berry G, Liang XH, Levine B, Herman B. 1998. Quantitative fluorescence resonance energy transfer measurements using fluorescence microscopy. *Biophys J* **74**(5):2702–2713.
36. Berney C, Danuser G. 2003. FRET or no FRET: a quantitative comparison. *Biophys J* **84**(6):3992–4010.
37. Ha T, Enderle T, Ogletree DF, Chemla DS, Selvin PR, Weiss S. 1996. Probing the interaction between two single molecules: fluorescence resonance energy transfer between a single donor and a single acceptor. *Proc Natl Acad Sci USA* **93**(13):6264–6268.

38. Kapanidis AN, Lee NK, Laurence TA, Doose S, Margeat E, Weiss S. 2004. Fluorescence-aided molecule sorting: analysis of structure and interactions by alternating-laser excitation of single molecules. *Proc Natl Acad Sci USA* **101**(24):8936–8941.
39. Lee NK, Kapanidis AN, Wang Y, Michalet X, Mukhopadhyay J, Ebright RH, Weiss S. 2005. Accurate FRET measurements within single diffusing biomolecules using alternating-laser excitation. *Biophys J* **88**(4):2939–2953.
40. Kapanidis AN, Lee NK, Laurence TA, Doose S, Margeat E, Weiss S. 2004. Fluorescence-aided molecule sorting: Analysis of structure and interactions by alternating-laser excitation of single molecules. *Proc Natl Acad Sci USA* **101**(24):8936–8941.
41. Fore S, Yuen Y, Hesselink L, Huser T. 2007. Pulsed-interleaved excitation FRET measurements on single duplex DNA molecules inside C-shaped nanoapertures. *Nanotechnol Lett* **7**(6):1749–1756.
42. Wolf DE. 1992. Theory of fluorescence recovery after photobleaching measurements on cylindrical surfaces. *Biophys J* **61**(2):487–493.
43. Magde D, Webb WW, Elson E. 1972. Thermodynamic fluctuations in a reacting system: measurement by fluorescence correlation spectroscopy. *Phys Rev Lett* **29**(11):705–707.
44. Magde D, Elson EL, Webb WW. 1974. Fluorescence correlation spectroscopy, II: an experimental realization. *Biopolymers* **13**(1):29–61.
45. Elson EL, Webb WW. 1975. Concentration correlation spectroscopy: a new biophysical probe based on occupation number fluctuations. *Annu Rev Biophys Bioeng* **4**:311–334.
46. Maiti S, Haupts U, Webb WW. 1997. Fluorescence correlation spectroscopy: diagnostics for sparse molecules. *Proc Natl Acad Sci USA* **94**(22):11753–11757.
47. Hess ST, Webb WW. 2002. Focal volume optics and experimental artifacts in confocal fluorescence correlation spectroscopy. *Biophys J* **83**(4):2300–2317.
48. Enderlein J, Gregor I, Patra D, Dertinger T, Kaupp UB. 2005. Performance of fluorescence correlation spectroscopy for measuring diffusion and concentration. *Chemphyschem* **6**(11):2324–2336.
49. Malvezzi-Campeggi F, Jahnz M, Heinze KG, Dittrich P, Schwille P. 2001. Light-induced flickering of DsRed provides evidence for distinct and interconvertible fluorescent states. *Biophys J* **81**(3):1776–1785.
50. Hollars CW, Lane SM, Huser T. 2003. Controlled non-classical photon emission from single conjugated polymer molecules. *Chem Phys Lett* **370**(3–4):393–398.
51. Fore S, Laurence TA, Yeh Y, Balhorn R, Hollars CW, Cosman M, Huser T. 2005. Distribution analysis of the photon correlation spectroscopy of discrete numbers of dye molecules conjugated to DNA. *IEEE J Sel Top Quantum Electron* **11**(4):873–880.
52. Huang Z, Thompson NL. 1996. Imaging fluorescence correlation spectroscopy: nonuniform IgE distributions on planar membranes. *Biophys J* **70**(4):2001–2007.
53. Wiseman PW, Petersen NO. 1999. Image correlation spectroscopy, II: optimization for ultrasensitive detection of preexisting platelet-derived growth factor-beta receptor oligomers on intact cells. *Biophys J* **76**(2):963–977.
54. Hebert B, Costantino S, Wiseman PW. 2005. Spatiotemporal image correlation spectroscopy (STICS) theory, verification, and application to protein velocity mapping in living CHO cells. *Biophys J* **88**(5):3601–3614.
55. Kolin DL, Costantino S, Wiseman PW. 2006. Sampling effects, noise, and photobleaching in temporal image correlation spectroscopy. *Biophys J* **90**(2):628–639.
56. Simons K, Ikonen E. 1997. Functional rafts in cell membranes. *Nature* **387**(6633):569–572.
57. Levene MJ, Korlach J, Turner SW, Foquet M, Craighead HG, Webb WW. 2003. Zero-mode waveguides for single-molecule analysis at high concentrations. *Science* **299**(5607):682–686.